Doctoral Dissertation

Studies on Fabrication of Inorganic Porous Materials Using Three-dimensional Cellulose Skeleton as Templates

三次元セルロース骨格をテンプレートとした無機多孔材料の作製に関する研究

LYU YANTING

June 2021

Graduate School of Engineering

Osaka University

Content

General Introduction

Inorganic materials with unique physical and chemical properties have attracted great attention because of their many promising applications in a wide range of fields, including electrochromic devices,[1] photocatalysis,[2] sensors,[3] batteries,[4] and solar cells.[5] Inorganic materials can be tailored to exhibit desired physical and chemical characteristics under given operating conditions (e.g., temperature, frequency, or pressure). To produce many of these inorganic materials, specific morphological structures, many of which imitate those found in nature, need to be obtained using synthetic materials.

Naturally occurring species are employed as resource for a wide range of materials which suggests that a significant fraction of complex functionalities of living systems are based on their hierarchical structures.[6] Hierarchically porous materials have already received much attention in biomedical and environmental applications owing to their high surface area, high pore volume ratios, excellent accessibility to active sites, and enhanced mass transport and diffusion.[7-10] Compared to conventional porous materials with uniform pore dimensions that can be adjusted over a wide range of length scales, hierarchical porous materials with well-defined pore dimensions and topologies offer minimized diffusive resistance to mass transport by macropores, and high surface area for active site dispersion over the micro- and/or mesopores.[11] For example, micro-/mesopores possess size or shape selectivity and high surface area for active site dispersion. The macropores act as flow-through channels and can minimize diffusive resistance to mass transport and provide easier access to the active sites.[7, 12] Therefore, hierarchical porous materials show superior properties for flow-through applications and enable fast separation without loss in efficiency and high-throughput screening.[13] Depending on the synthetic strategies, the pores might be arranged and connected in very different ways as schematically shown in **Figure 1**.[14]

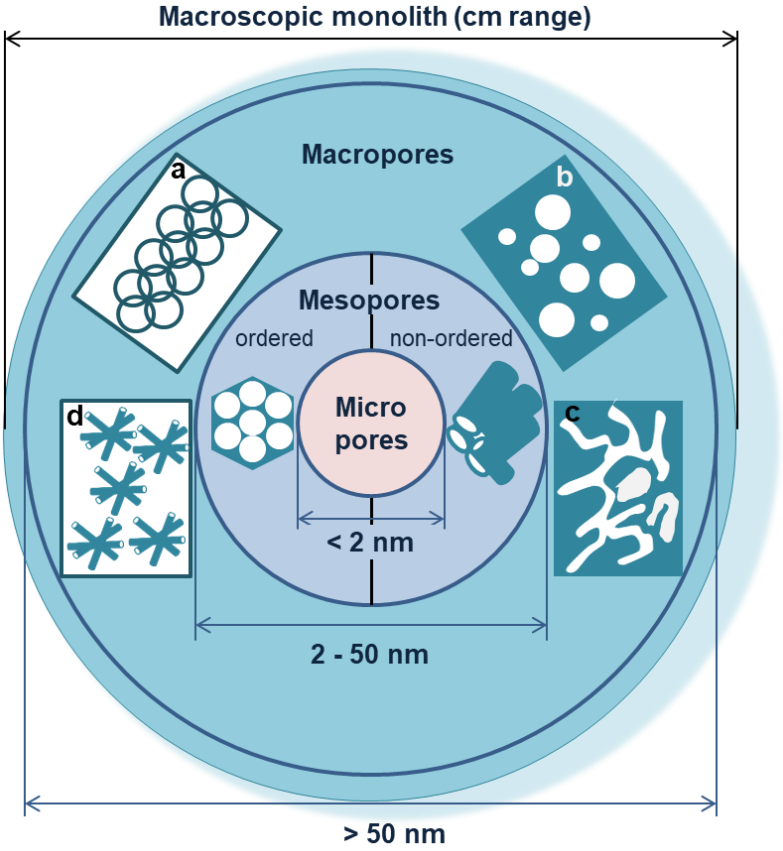

Figure 1 Concept of hierarchy in a porous material: schematics of a hierarchical porous build-up from the micrometer scale, via the mesoscopic regime to the macroscopic porous dimension within a monolithic material: In the macroporous regime, the different pore arrangements, such as inverse opal-like structures (a), isolated pores (b), co-continuous porosity (c), and a cellular build-up (d) are shown (in the scheme, the blue part represents the solid network, the white part is the pore space). For the mesoporous regime, either well-organized pores with monomodal character as shown for a 2D hexagonal structure or disordered arrangements are possible.

In the past two decades, numerous hierarchical porous monolithic materials were developed for applications in liquid separations,[15] catalysis,[16] and bioengineering.[17] Since their introduction in the field of chromatography in the 1990's, monoliths have emerged as an alternative to particulate packing materials, mainly because the continuous bed allows percolation of mobile phase through it at high linear velocities without excessive backpressure. They were divided into three categories according to their chemical composition: inorganic, organic, and hybrid hierarchical porous monolithic materials that combined the characteristic of both inorganic and organic materials, as shown in **Figure 2**. These classes are differentiated

by their morphology and physicochemical properties. Generally, monoliths are relatively easy to synthesize, even with controlled pore size distribution, and they may be further functionalized aiming at specific applications.[18] The unique properties of monoliths, such as the high number of different surface chemistry properties, and their tolerance to high flow rates, thus yielding fast chromatographic separations at acceptable backpressure, make them superior in some applications. Traditionally, monoliths are employed in liquid-phase separations, mainly liquid chromatography and related miniaturized techniques, such as capillary liquid chromatography (CLC) and electrochromatography (CEC).[19, 20] More recently, monoliths have been applied in other miniaturized systems, in which the reduced dimensions of columns minimize both shrinkage and swelling, beyond facilitating the *in situ* molding of the stationary phase within the capillary columns.

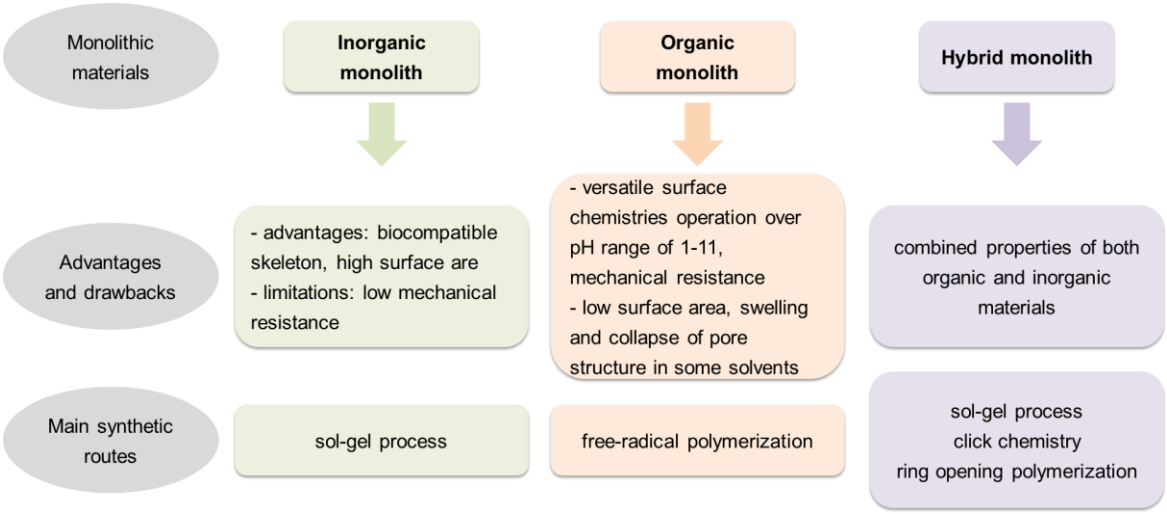

Figure 2 The categories and characteristics of monolithic materials.

Polymeric monoliths can be synthesized to have good mechanical stability, biocompatibility, high porosity, chemical resistivity, sufficient access sites for ligand-target interaction and low back pressure for high throughput application of micro-and macromolecules.[21] The shape and size of the mould dictates the final monolithic-polymer formed and the pattern of the flow hydrodynamics. Different architectural shapes synthesized for polymer monoliths include annular, cylindrical, conical and disk.[22] Various types of

polymeric monoliths can be synthesized based on the type of monomers and/or polymerization process employed for synthesis, and they can be molecularly engineered to possess varying physicochemical properties. Hierarchically porous monoliths of cellulose,[23] poly(acrylonitrile),[24] poly(vinyl alcohol),[25] poly(ethylene-co-vinyl alcohol),[26] poly(vinyl alcohol) monolith,[27] and poly(γ -glutamic acid)[28] were successfully prepared by selecting an appropriate condition. These monoliths contained uniform mesopores as well as sub-micron or micron-sized macropores. The monoliths were obtained using simple processes, namely, solubilization of the polymer powder into a mixture of solvents by heating and subsequent cooling of the solution, during which phase separation took place to form the monolith. The structure of the polymer monoliths can be well adjusted by controlling the preparation parameters such as temperature, polymerization time, presence of oxygen, initiator concentration, monomer-porogen ratio and con-centration, which have been identified to have effects on the porosity, morphology, physicochemical properties, hydro-dynamic and mass transfer characteristics of the monoliths in relation to analyses. Polymeric monoliths such as poly(methacrylate) have functional moieties on their interconnected pores that can be activated for ligand immobilization, allowing a variety of activation chemistries to be applied for the formation of covalent and non-covalent bonding with ligands.[21] Several researchers have discussed research advancements made in the synthesis and application of polymeric monoliths for small molecule applications in an isocratic mode,[29] fast biomolecule isolation,[30] and preparative chromatography.[31] In the past, because of the low surface area, organic polymeric monoliths were more suitable for separation of large molecules.[32] Recently, efforts have been made to overcome this hindrance and several applications for separation of small molecules have been presented.[33]

Hybrid monoliths, whose structure shows organic and inorganic moieties, arose as alternatives materials because of the easy preparation, high pH tolerance, and good mechanical stability.[34] Moreover, common drawbacks such as solvent swelling (for porous

polymers) and tedious functionalization (for inorganic phases) are avoided, the latter because of the addition of functionalized monomers during the synthesis.[35] For example, cellulose/TiO_2 monolith,[36] and MS@TiO_2@PPy monoliths[37] were prepared as photocatalytic materials. Multiwall carbon nanotube, functionalized with sulfonate group (MWCNTs-SO_3^-) incorporated in PVA cryogel has been developed and used as an SPE sorbent to separate b-agonists from animal feeds [38] and molecularly imprinted polymer (MIP) composite cryogel was used to separate propranolol from complex sample.[39] Polypyrrole-coated GO that was incorporated into a PVA cryogel as a newly-designed hybrid monolith sorbent for the extraction and preconcentration of trace sulfonamides.[40] Generally, organic or inorganic-organic monoliths are resistant to pH, biocompatible, easy to synthesize mostly via polymerization and possess high interconnectivities.[41] However, polymer-based materials are limited in their applicability due to calcination at temperatures well below 200 °C and are inadequate as catalyst support for many organocatalytic reactions due to dissolving in most organic solvents. Additionally, due to their low surface area, polymer based monolithic phases are much more commonly applied to the separation of large bio-molecules rather than small molecules. For these reasons, hierarchically porous monolithic inorganic materials are potential candidates for more applications in flow system.

Such a novel type of interconnected porous inorganic materials with a 3D network is currently attracting a great degree of interest due to their potential technological application. Of the numerous methods for preparation of inorganic materials (such as inorganic oxides), sol-gel methods using metal alkoxides as raw materials have been shown to be a particularly promising approach owing to advantages such as low cost, ambient operating conditions, and an easy one-pot processing route.[42] In the sol-gel process, hydrolysis and condensation reactions of metal alkoxides are preferentially incorporated into one of the blocks through hydrogen bonds. Condensation reactions of hydrolysable precursors, e.g. metal or semimetal alkoxides, but also salts, induced by the controlled addition of water represent the key steps in

the synthesis of monolithic materials. The network evolves via nucleation and growth of nanometer-sized sol particles as well as their aggregation. Accordingly, reaction conditions, such as the choice of the precursor, its concentration, pH value, temperature, solvent, etc., are selected to simultaneously form co-continuous structures, resulting in a network structure, the network chemistry and pore structure (from polymeric to particulate networks of either small or large particles, etc.) of inorganic-material skeletons.[43] However, it is difficult to maintain a porous structure because their synthesis often involves a complicated phase separation in sol–gel reactions. The formation of 3D structures from nanomaterials remains a challenge mainly due to the limited ability to form hierarchical 3D structures by a large scale, low cost, and facile process. [44] 3D printing technology is a powerful additive manufacturing approach for fast, accurate, and customized fabrication of objects with complex geometries, in the macro-, meso-, and microscales. In recent years, 3D printing also used in preparation of hierarchical porous monolithic inorganic materials such as silica,[45] graphene oxide,[46] zeolite,[47] and so on. The most commonly used synthetic technique for the fabrication of inorganic materials is hard templating, where a hierarchical structured polymer is used as a template, followed by carbonization of the composite and subsequent removal of the template.[17, 48, 49] Templating involves using one material, the template, to dictate a specific shape for another material with the desired morphology. The template assumes a specific shape and then a second material, the precursor, is introduced (**Figure 3**). The precursor is confined by the template and fills in the voids. In the final shape, these two materials can be kept, or the original template material can be removed.[50] The template can be divided into bio-template and artificial template.

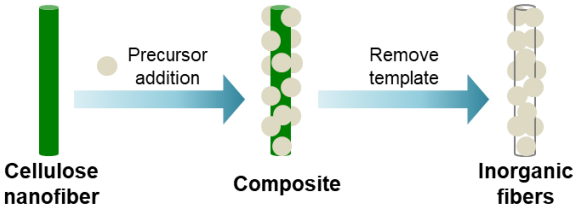

Figure 3 Graphical illustration depicting the process of templating.

Nature employs an enormous variety of scaffolds upon which identical 3D structures form which cannot be easily mimicked artificially.[51, 52] Up to date, biotemplates have been

widely used to create 3D structures. Furthermore, the achievements of very primitive organisms in terms of their synthesis and control of morphology are really remarkable and tremendous knowledge is still unrevealed. The biotemplates present several advantages compared to the artificial ones, mainly, due to their abundance (they are accumulated in mass quantities), morphological diversity, identical structures, and large size (from a few mm to a few cm).[37] Moreover, modification of the compositions of the biotemplates is usually facile and general. For example, Otsuka and co-workers used the shell of *Calcarina baculatus* as a carbonate precursor to obtain tricalcium phosphate (β-TCP) and Zn-TCP via a hydrothermal process in which carbonate and calcium are replaced by phosphate and zinc ions, respectively.[53] 3D diatom/MnO_2 and MnO_2 replica structures with unique diatom morphologies were prepared using diatoms as templates and the samples show promising application as supercapacitor electrode materials.[54] However, to produce many of these advanced materials, specific morphological structures, many of which imitate those found in nature, need to be obtained using synthetic materials.

Cellulose monoliths, as a result of their monolithic and hierarchically porous structure, possess several features such as hydrophilicity, easy chemical modification, large surface area, insolubility in water and common organic solvents, and high mechanical strength.[55] Additionally, hierarchically porous cellulose monoliths exhibiting high hydrophilicity and tolerance toward common solvents can be easily fabricated from a cellulose acetate solution by thermally induced phase separation (TIPS).[23] Unlike crystalline cellulose, cellulose acetate is a commercially available derivative of cellulose. Owing to the partial acetylation of their hydroxyl groups on the side chains, cellulose acetate shows a good solubility toward some organic solvents such as acetone and DMF. Therefore, the porous cellulose acetate monolith can be easily fabricated through a dissolution and phase separation induced by temperature. In this method, the morphology of the final cellulose acetate monolith can be controlled by changing the conditions such as the initial cellulose acetate concentration and quench

temperature. After deacetylation, the cellulose monolith can be easily obtained. The cellulose monolith prepared via TIPS has a hierarchically porous structure (**Figure 4**). This method escapes from the chemical crosslinking steps and the product kept the original chemical structure of cellulose. Utilizing the hydrophilic but water-insoluble properties of cellulose monoliths, it is possible to incorporate the metal alkoxides or inorganic slurry into the monolith skeleton during the reaction.

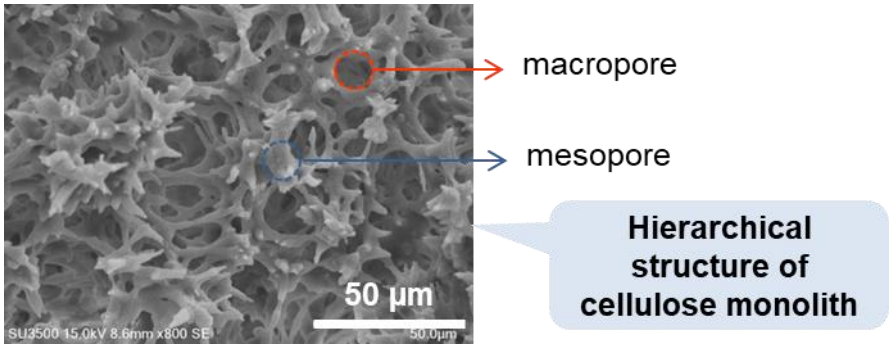

Figure 4 SEM image of the cellulose monolith prepared via TIPS.

In this thesis, the author aimed at the develop efficient strategies for fabricating hierarchically porous inorganic materials using the cellulose materials and commercial cellulose-based materials as templates. Specifically, the cellulose monolith prepared via TIPS will be used as the main template in this research, and then different monolithic inorganic materials were prepared. Chapter 1 describes the preparation of porous inorganic materials by using cellulose skeleton as template. Chapter 2 focuses on the preparation of hierarchical TiO_2 monolith by using cellulose monolith as template. And the photocatalytic performance of the TiO_2 monolith was evaluated by studying its effect on the degradation of methylene blue (MB) in flow system. Chapter 3 aims at the fabrication of inorganic oxide fiber using a cigarette filter as template. This method provides a clean method to convert waste materials to a useful template for inorganic oxides with relatively simple steps, and the resulting product shows great potential for water treatment. These fabrication strategies established in this thesis may provide a guidance for the future fabricate hierarchically porous inorganic materials based on

biodegradable monolithic cellulose materials or commercial cellulose-based materials. We also believe that the prepared hierarchically porous inorganic materials are promising in other application and further modification.

Outline of this thesis

In this thesis, the author aimed at the development of efficient strategies for fabricating hierarchically porous inorganic materials using the cellulose materials and commercial cellulose-based materials as templates. This thesis includes 3 chapters.

Chapter 1 Porous inorganic materials prepared using cellulose skeleton as template

In this chapter, for the first time, we used an ecofriendly cellulose material as a template to prepare a hydrophilic and hierarchically porous silica monolith. The cellulose monolith template was prepared from cellulose acetate by a thermally induced phase separation method. The silica was then prepared in the presence of the cellulose monolith by a typical sol-gel reaction of tetraethyl orthosilicate (TEOS) to form the composite monolith, which was converted to the silica monolith by burning in air to remove the cellulose monolith. Owing to the hierarchically porous structure of the cellulose monolith template, the obtained silica monolith showed a similar hierarchically porous structure. The surface-modified silica monolith was developed for further applications. Moreover, the recycled cigarette filters are deacetylated to cellulose filters (CFs), which are then applied as a template to prepare fiber-like inorganic oxides (TiO_2 and SiO_2). The obtained inorganic oxides (TiO_2 and SiO_2) show a similar fiber-like structure to the CF template. Furthermore, the TiO_2 fiber-like materials are evaluated for their photocatalytic properties by analyzing their effect on the degradation of methylene blue (MB) as model pollutants.

Chapter 2 Hierarchical porous TiO_2 monolith prepared using cellulose monolith as

template

In this part of research, hierarchically porous TiO_2 monolithic materials are potential candidates for water remediation, as they are easy to recover and can be used in flow systems. In this study, we used an ecofriendly cellulose material as a template to prepare a hierarchically porous TiO_2 monolith. The cellulose monolith template was prepared from cellulose acetate by a thermally induced phase separation method. A composite monolith was then prepared in the presence of the cellulose monolith by a typical sol–gel reaction of titanium isopropoxide (TTIP). This composite monolith was then converted to a TiO_2 monolith by burning in air to remove the cellulose monolith. Owing to the hierarchically porous structure of the cellulose monolith template, the obtained TiO_2 monolith showed a similar hierarchically porous structure. The pore structure could be controlled by changing the fabrication parameters, such as the type of cellulose monolith and TTIP content. The photocatalytic performance of the TiO_2 monolith was evaluated by studying its effect on the degradation of methylene blue (MB) in flow system.

Chapter 3 Facile synthesis of three-dimensional hydroxyapatite monolith for protein adsorption

In Chapter 3, Hydroxyapatite (HA) shows promising applications in clinical treatment of bone defects owing to its excellent physicochemical properties, such as biocompatibility, bioactivity, and osteoconductivity. However, it is difficult to maintain a porous structure in HA monoliths because the processing difficulty. Herein, a hard template method was developed and a porous HA monolith with hierarchical pore structure, suitable porosity and pore size was successfully prepared. The cellulose monolith template was prepared from cellulose acetate by a thermally induced phase separation method. The cellulose monoliths were then immersed into the HA slurry with chitosan to form the composite monolith, which was converted to the HA monolith by burning in air to remove the chitosan and cellulose

monolith. Owing to the hierarchically porous structure of the cellulose monolith template, the obtained HA monolith showed a similar hierarchically porous structure, as confirmed by scanning electron microscopy and nitrogen adsorption-desorption analyses. Furthermore, the as-prepared HA monolith was explored to study the adsorption property of bovine serum albumin (BSA), and the adsorption evaluation indicated that HA monolith has a high adsorption capacity of BSA.

References

1. L. Santos, P. Wojcik, J. V. Pinto, E. Elangovan, J. Viegas, L. Pereira, R. Martins and E. Fortunato, *Adv. Electron. Mater.*, 2015, **1**, 1400002.

2. S. Wooh, N. Encinas, D. Vollmer and H. J. Butt, *Adv. Mater.*, 2017, **29**, 1604637.

3. J. Bai and B. X. Zhou, *Chem. Rev.*, 2014, **114**, 10131-10176.

4. K. K. Banger, Y. Yamashita, K. Mori, R. L. Peterson, T. Leedham, J. Rickard and H. Sirringhaus, *Nat. Mater.*, 2011, **10**, 45-50.

5. J. J. Lin, Y. U. Heo, A. Nattestad, Z. Q. Sun, L. Z. Wang, J. H. Kim and S. X. Dou, *Sci. Rep.*, 2014, **4**, 5769.

6. J. Aizenberg, J. C. Weaver, M. S. Thanawala, V. C. Sundar, D. E. Morse and P. Fratzl, *Science*, 2005, **309**, 275-278.

7. S. Dutta, A. Bhaumik and K. C. W. Wu, *Energy Environ. Sci.*, 2014, **7**, 3574-3592.

8. J. Xiao, D. H. Mei, X. L. Li, W. Xu, D. Y. Wang, G. L. Graff, W. D. Bennett, Z. M. Nie, L. V. Saraf, I. A. Aksay, J. Liu and J. G. Zhang, *Nano Lett.*, 2011, **11**, 5071-5078.

9. Z. C. Wu, K. Tian, T. Huang, W. Hu, F. F. Xie, J. J. Wang, M. X. Su and L. Li, *ACS Appl. Mater. Interfaces*, 2018, **10**, 11108-11115.

10. T. Huang, Z. C. Wu, Q. Yu, D. G. Tan and L. Li, *Chem. Eng. J.*, 2019, **359**, 69-78.

11. C. Zou, D. C. Wu, M. Z. Li, Q. C. Zeng, F. Xu, Z. Y. Huang and R. W. Fu, *J. Mater. Chem.*, 2010, **20**, 10945-10945.

12. Z. S. Liu, P. Jiang, G. Huang, X. W. Yan and X. F. Li, *Anal. Chem.*, 2019, **91**, 3659-3666.

13. G. Beck, M. Sieland, J. F. Beleites, R. Marschall and B. M. Smarsly, *Inorg. Chem.*, 2019, **58**, 2599-2609.

14. A. Feinle, M. S. Elsaesser and N. Husing, *Chem. Soc. Rev.*, 2016, **45**, 3377-3399.

15. X. M. Qin, B. Wang, X. Zhang, Y. T. Shi, S. H. Ye, Y. Z. Feng, C. T. Liu and C. Y. Shen, *Ind. Eng. Chem. Res.*, 2019, **58**, 20291-20299.

16. L. X. Tan and B. E. Tan, *Chem. Eng. J.*, 2020, **390**, 124485.

17. K. Zhou, P. Yu, X. J. Shi, T. X. Ling, W. N. Zeng, A. J. Chen, W. Yang and Z. K. Zhou, *ACS Nano*, 2019, **13**, 9595-9606.

18. H. Q. Wang, Z. Li, Q. Niu, J. T. Ma and Q. Jia, *Appl. Surf. Sci.*, 2015, **353**, 1326-1333.

19. D. S. Xu, H. K. Shao, R. Y. Luo, Q. Q. Wang, E. Sanchez-Lopez, S. Fanali, M. L. Marina and Z. J. Jiang, *J. Chromatogr. A*, 2018, **1557**, 43-50.

20. J. J. Ou, Z. S. Liu, H. W. Wang, H. Lin, J. Dong and H. F. Zou, *Electrophoresis*, 2015, **36**, 62-75.

21. V. Pichon, F. Brothier and A. Combes, *Anal. Bioanal. Chem.*. 2015, **407**, 681-698.

22. E. L. Pfaunmiller, M. L. Paulemond, C. M. Dupper and D. S. Hage, *Anal. Bioanal. Chem.*. 2013, **405**, 2133-2145.

23. Y. R. Xin, Q. C. Xiong, Q. H. Bai, M. Miyamoto, C. Li, Y. H. Shen and H. Uyama, *Carbohydr. Polym.*, 2017, **157**, 429-437.

24. K. Okada, M. Nandi, J. Maruyama, T. Oka, T. Tsujimoto, K. Kondoh and H. Uyama, *Chem. Comm.*, 2011, **47**, 7422-7424.

25. X. X. Sun, T. Fujimoto and H. Uyama, *Polym J*, 2013, **45**, 1101-1106.

26. G. W. Wang, H. Yoshikawa, E. Tamiya and H. Uyama, *RSC Adv.*, 2015, **5**, 25777-25780.

27. X. X. Sun, G. W. Sun and X. H. Wang, *Polymer*, 2017, **108**, 432-441.

28. S. B. Park, T. Fujimoto, E. Mizohata, T. Inoue, M. H. Sung and H. Uyama, *J. Microbiol. Biotechnol.*, 2013, **23**, 942-952.

29. F. Svec, *J. Chromatogr. A*, 2012, **1228**, 250-262.

30. A. Podgornik and N. L. Krajnc, *J. Sep. Sci.*, 2012, **35**, 3059-3072.

31. C. M. Ongkudon, T. Kansil and C. Wong, *J. Sep. Sci.*, 2014, **37**, 455-464.

32. R. D. Arrua, M. Talebi, T. J. Causon and E. F. Hilder, *Anal. Chim. Acta*, 2012, **738**, 1-12.

33. M. R. Gama, P. Aggarwal, M. L. Lee and C. B. G. Bottoli, *Electrophoresis*, 2017, **38**, 3029-3035.

34. Z. Zajickova, *J. Sep. Sci.*, 2017, **40**, 25-48.

35. S. J. Liu, J. X. Peng, Z. Y. Liu, Z. S. Liu, H. Y. Zhang and R. A. Wu, *Sci. Rep.*, 2016, **6**, 34718.

36. M. A. Lucchini, E. Lizundia, S. Moser, M. Niederberger and G. Nystrom, *ACS Appl. Mater. Interfaces*, 2018, **10**, 29599-29607.

37. S. W. Yan, Y. Li, F. Xie, J. Wu, X. H. Jia, J. Yang, H. J. Song and Z. Z. Zhang, *ACS Sustain. Chem. Eng.*, 2020, **8**, 5347-5359.

38. S. Noosang, O. Bunkoed, P. Thavarungkul and P. Kanatharana, *J. Sep. Sci.*, 2015, **38**, 1951-1958.

39. S. Hajizadeh, C. G. Xu, H. Kirsebom, L. Ye and B. Mattiasson, *J. Chromatogr. A*, 2013, **1274**, 6-12.

40. K. Chullasat, P. Nurerk, P. Kanatharana, P. Kueseng, T. Sukchuay and O. Bunkoed, *Anal. Chim. Acta*, 2017, **961**, 59-66.

41. Z. Walsh, B. Paull and M. Macka, *Anal. Chim. Acta*, 2012, **750**, 28-47.

42. T. M. Budnyak, I. V. Pylypchuk, V. A. Tertykh, E. S. Yanovska and D. Kolodynska, *Nanoscale Res. Lett.*, 2015, **10**, 87.

43. S. S. Yin, L. Song, S. L. Xia, Y. J. Cheng, N. Hohn, W. Chen, K. Wang, W. Cao, S. J. Hou and P. Muller-Buschbaum, *Small Methods*, 2020, **4**, 1900689.
44. M. Diab and T. Mokari, *Adv. Mater.*, 2018, **30**, 1706349.
45. E. S. Farrell, Y. Schilt, M. Y. Moshkovitz, Y. Levi-Kalisman, U. Raviv and S. Magdassi, *Nano Lett.*, 2020, **20**, 6598-6605.
46. J. H. Ma, P. Wang, L. Dong, Y. B. Ruan and H. B. Lu, *J. Colloid Interface Sci.*, 2019, **534**, 12-19.
47. H. M. Zhang, P. F. Wang, H. Zhang, H. Yang, H. Y. Wang and L. Zhang, *Ind. Eng. Chem. Res.*, 2020, **59**, 8223-8229.
48. S. Y. Chen, B. H. Zhou, W. L. Hu, W. Zhang, N. Yin and H. P. Wang, *Carbohydr. Polym.*, 2013, **92**, 1953-1959.
49. C. Busuioc, C. D. Ghitulica, A. Stoica, M. Stroescu, G. Voicu, V. Ionita, L. Averous and S. I. Jinga, *Ceram. Int.*, 2018, **44**, 9433-9441.
50. M. E. Lamm, K. Li, J. Qian, L. Wang, N. Lavoine, R. Newman, D. J. Gardner, T. Li, L. B. Hu, A. J. Ragauskas, H. Tekinalp, V. Kunc and S. Ozcan, *Adv. Mater.*, 2021, **33**, 2005538.
51. A. R. Studart, *Chem. Soc. Rev.*, 2016, **45**, 359-376.
52. C. Q. Zhang, D. A. Mcadams and J. C. Grunlan, *Adv. Mater.*, 2016, **28**, 6292-6321.
53. J. Chou, T. Ito, M. Otsuka, B. Ben-Nissan and B. Milthorpe, *Adv. Healthc. Mater.*, 2013, **2**, 678-681.
54. F. Li, Y. Xing, M. Huang, K. L. Li, T. T. Yu, Y. X. Zhang and D. Losic, *J. Mater. Chem. A*, 2015, **3**, 7855-7861.
55. Z. T. Xie, T. A. Asoh and H. Uyama, *Carbohydr. Polym.*, 2019, **214**, 195-203.

Chapter 1.

Porous inorganic materials prepared using cellulose skeleton as template

1.1 Introduction

Silica monoliths with a continuous porous structure have received much attention in biomedical and environmental applications owing to their high-performance separation/adsorption behaviors. Their hierarchically porous structure can offer the benefits of each pore size combined in a single structure. For example, the micro- or mesopores possess size or shape selectivity and a large surface area; moreover, the macropores provide easier access to the active sites and reduce the pressure drop over the material.[1] With a large surface area and controllable pore architecture, hierarchically porous silica materials have been employed in various fields, such as catalysis,[2] drug delivery,[3] ion or molecule adsorption,[4] and separation.[5]

In general, sol-gel methods are often used to prepare silica materials because of their mild conditions, such as relatively low temperature and pressure.[6] The chemical reaction of an alkoxysilane to silica is typically caused by two kinds of reactions: hydrolysis and polycondensation, starting from $Si(OR)_4$ to form Si-O-Si bonds in silica oligomers and polymers.[7-9] In the sol-gel process, reaction conditions are selected to simultaneously form the co-continuous structures, resulting in a network structure of silica gel skeletons with macropores. Additives, which include water-soluble polymers and surfactants, can also be used to induce phase separation. The silica gel skeletons of a macroporous network structure thus formed actually contain micropores, which are subsequently enlarged by treatment with ammonia to form mesoporous skeletons.[10] However, it is difficult to maintain a porous structure in silica monoliths because their synthesis often involves complicated phase separation in sol-gel reactions. Moreover, the preparation of silica monoliths is cumbersome, has poor controllability, and usually requires a long aging time.[11, 12] In this case, monolithic silica is prepared by the hydrolysis and polycondensation of alkoxysilane

in the presence of poly(ethylene oxide) (PEO).[13] Tetramethyl orthosilicate (TMOS) is added to acetic acid/PEO to form a homogeneous solution, which is then poured into a plastic mold to prepare the silica monolith.[14] A mesoporous and macroporous silica monolith is also obtained using fibroin nanofibers as the sacrificial scaffold that is selectively removed from the monolith by thermal treatment.[15]

On the other hand, cellulose monoliths possess several features such as hydrophilicity, easy chemical modification, large surface area, insolubility in water or common organic solvents, and high mechanical strength as a result of the monolithic and hierarchically porous structure.[16] Additionally, hierarchically porous cellulose monoliths exhibiting high hydrophilicity and tolerance toward common solvents are easily fabricated from a cellulose acetate (CA) solution by thermally induced phase separation (TIPS).[17] Utilizing the hydrophilic but water-insoluble properties of cellulose monoliths, it is possible to incorporate the silica precursor into the monolith skeleton during the sol-gel reaction.

Cellulose-based materials are used in numerous industrial products, many of them, such as cellulose acetate-based cigarette filters, are disposed of after usage, posing a waste disposal and environmental pollution hazard.[18] The number of cigarette filters disposed of annually on a global basis is estimated to be up to 5.6 trillion,[19] and the number is increasing annually. Moreover, cigarette filters do not biodegrade easily.[20] Fortunately, unlike many materials that end up mixed with other types of waste, it is possible to collect and reutilize cigarette filters because they are mainly disposed of in designated smoking areas.[21] Inspired by the concept of sustainable chemistry and engineering, some researches have attempted to convert cigarette filters into valuable products. All the previously mentioned treatments of waste cigarette filters provide useful ways to reuse waste cigarette filters. Most of the reuse of waste cigarette filters usually focused on one aspect (morphology or chemical properties), and few studies have utilized the combination of cigarette filters morphology and chemical properties. Therefore, it is expected that more reasonable and effective methods can be used to develop high value-added materials that simultaneously utilize the morphology and chemical properties of cigarette filters.

Cigarette filters, which mainly composed of cellulose acetate, can be deacetylated into cellulose filters (CFs). On the other hand, the fibrous CFs can be easily converted into the fibrous structure of inorganic oxide by subjecting an appropriate amount of metal alkoxide to a sol-gel reaction and then removing the template. Therefore, recycling cellulose acetate cigarette filters and using them as templates to prepare inorganic oxides not only reduces environmental pressure, but also produces value-added products.

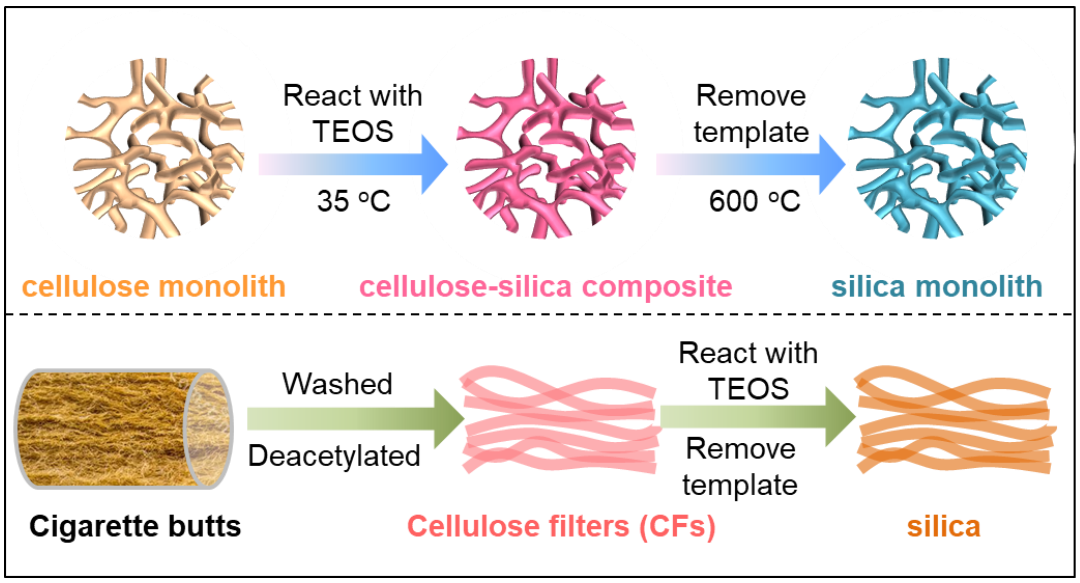

Figure 1-1 The scheme of the preparation process of silica materials by using cellulose monolith and cellulose filter (CF) as template, respectively.

Herein, for the first time, we used an ecofriendly cellulose monolith as a template to prepare a hydrophilic and hierarchically porous silica monolith (**Figure 1-1**). The silica monolith was prepared in the presence of a cellulose monolith by a typical sol-gel reaction of tetraethyl orthosilicate (TEOS). Hydrolysis and condensation reactions of the TEOS occur during the sol-gel process.[22] Finally, the silica monolith was obtained by burning the composite monolith in air to remove the cellulose template. Owing to the hierarchically porous structure of the cellulose monolith template, the obtained silica monolith showed a similar hierarchically porous structure. The pore structure could be controlled by changing the fabrication parameters such as the kind of cellulose monolith and TEOS concentration. Furthermore, the surface-modified silica monolith was developed for further

applications. Moreover, recycled cellulose acetate filters (CAFs) were deacetylated to cellulose filters (CFs), and then applied as a template to prepare fiber-like inorganic oxides (TiO_2 and SiO_2) (**Figure 1-1**), the prepared inorganic oxides (TiO_2 and SiO_2) exhibited a similar fibrous structure to the CF template. Moreover, the obtained inorganic oxides (TiO_2 and SiO_2) exhibited high surface area and pore volume. The TiO_2 fiber-like materials were evaluated for their photocatalytic properties by analyzing the methylene blue (MB) and methyl orange (MO) degradation.

1.2 Experimental

Materials

Cellulose acetate powder (CA, L_{30}) with an acetylation degree of 55% was kindly provided by Daicel Co., Ltd. Japan. Cellulose acetate filters (CAFs) from PEACE-Super Light cigarettes (Japan Tobacco Inc., Japan) were collected from cigarette butts consumed by our laboratory mates. The covering paper and tobacco ash on the CAFs were manually detached. Cetyltrimethylammonium bromide (CTAB) was purchased from Nacalai Tesque, Inc. 3-aminopropyltrimethoxysilane (APTMS), titanium isopropoxide (TTIP), tetraethyl orthosilicate (TEOS), and isopropyl alcohol were purchased from Tokyo Chemical Industry Co., Ltd. Titanium (IV) oxide (P25) was purchased from Fujifilm Wako Pure Chemical Corporation. All other chemicals used were chemically purified and purchased commercially.

Preparation of cellulose monolith

The cellulose acetate monolith and cellulose monolith were prepared *via* the TIPS method reported in a previous work.[17] Cellulose acetate (2.0, 2.5, 3.0, and 3.5 g) was dissolved in 10 mL of dimethylformamide (DMF) at 90 °C. When the solution was completely dissolved by stirring, 15 mL of 1-hexanol was added gradually. After continuous stirring, the mixture became clear, and was then transferred into a mold and kept at 20 °C over 6 h to induce phase separation in order to obtain the cellulose acetate monolith. The cellulose monolith was then obtained by deacetylation under alkaline conditions (0.5 mol/L NaOH in methanol) for 3 h. Finally, the dried cellulose monolith was obtained by vacuum drying. The cellulose monolith prepared with different concentrations of cellulose acetate was designated as cellulose *x* monolith, in which *x* refers to the concentration of cellulose acetate.

Preparation of CFs

The CAFs were washed with 100 mL ethanol in a shaker for 3 h to remove any impurities. During the washing process, the solution was exchanged with fresh ethanol every hour until the solution became clear. After drying under a vacuum, the obtained CAFs with a length of approximately 25 mm were fixed in a heat-shrinkable

tube. 0.5 M NaOH/methanol solution (40 mL) was circulated through the tube using a peristaltic pump (EYELA, MP-1000) at a flow rate of 3 mL min^{-1} to react with the CAFs for 1 h. As a result, the CAFs were deacetylated to form CFs.[23]

Preparation of silica materials

The cellulose-silica monolith was prepared via a sol-gel reaction in the presence of the cellulose monolith. CTAB (0.05 g) was dissolved in 8 mL of deionized water by stirring. Subsequently, 0.15 mL of aqueous ammonia solution (28 wt%) was added to form a clear solution. Next, the CTAB/ammonia solution was added to the cellulose monolith (0.50 g), which was immersed in a continuously stirred solution of n-hexane (1 mL) and TEOS at 35 °C. After stirring for 12 h, the product was washed with deionized water and ethanol, following which the cellulose x-silica y monolith was obtained by vacuum drying for 3 h; x refers to the concentration of cellulose acetate (mg/mL) and y refers to the content of TEOS (%). For removal of the cellulose monolith, the cellulose-silica monolith was burned in air (increasing from room temperature to 600 °C at a rate of 5 °C/min), maintained at 600 °C for 2 h, then cooled to room temperature to prepare the silica x_y monolith. The control composite was prepared using the above method, with the exception that the cellulose monolith was replaced by a cellulose acetate monolith. The SiO_2 fiber-like was prepared using the above method, with the exception that the cellulose monolith template was replaced by a CF, the prepared sample was named as SiO_2-*x* fiber-like material (y refers to the content of TEOS (%)).

Surface modification of silica monolith

An amino-modified silica monolith was prepared using a silane coupling agent to modify the surface of the silica monolith. APTMS (0.75 g) was dissolved into 10 g of deionized water for 30 min. The silica monolith (1 g) was added into the APTMS aqueous solution, and the reaction was carried out at 65 °C for 16 h.[24] After the reaction, the product was washed with deionized water and ethanol, and the dried amino-modified silica monolith was obtained by freeze drying for 24 h.

Preparation of TiO_2 fiber-like material

CF-TiO_2 was prepared via a sol-gel reaction in the presence of CF. TTIP was

added to isopropyl alcohol and stirred for 20 min. Then, the CF was immersed in the TTIP/isopropyl alcohol solution. Subsequently, deionized water was added to the mixture under vigorous stirring. The volume ratio of isopropyl alcohol to water was 1:10, the total volume of the solution after adding distilled water was 15 mL, and the TTIP content was defined as the ratio of the TTIP volume to the total volume of the solution. The solution was subsequently heated to 80 °C for 5 h and cooled to room temperature, following which, the CF-TiO_2-*x* was washed with distilled water and dried at 80 °C, where *x* refers to the content of TTIP (%). To remove the CF, the CF-TiO_2 was burned in air (heating from room temperature to 500 °C at a rate of 1 °C min^{-1}), maintained at 500 °C for 2 h, and then cooled to room temperature to prepare the TiO_2-*x* fiber-like material.

Characteristics

Fourier transform infrared (FT-IR) measurement of the samples was performed using a Thermo Scientific Nicolet iS5 spectrometer equipped with an iD5 ATR attachment. The morphology of the monoliths was investigated by scanning electron microscopy (SEM) using a Hitachi S-3000N scanning electron microscope operated at 15 kV. The surface elemental composition was captured by energy-dispersive X-ray spectroscopy (EDS, Hitachi, Miniscope TM3000 equipped with SwiftED 3000). The Brunauer-Emmett-Teller (BET) surface area was studied by nitrogen adsorption-desorption analysis (Quantachrome Instruments). Samples were vacuum-degassed at 70 °C for 24 h prior to measurement. The pore diameter distribution and pore volume were obtained using the density functional theory (DFT). Thermogravimetric analysis (TGA) was conducted with a thermogravimetric analyzer (Hitachi, STA7200RV) in the temperature range of 40 to 800 °C at a heating rate 10 °C/min under nitrogen protection. Powder X-ray diffraction (XRD) patterns were obtained using a SmartLab (In-plane, Rigaku Corporation, Japan) with a Cu K-beta X-ray source and a scanning speed of 5° min^{-1} over a 2θ range of 5–80°. The generator voltage and current were 45 kV and 200 mA, respectively.

To measure the permeability of the monolith, it was tightly fitted with a heat shrink tubing and was then connected to a digital quantitative tubing pump (As One,

DSP-100SA) and a digital pressure gauge (Krone, KDM30). The value of the permeability coefficient, B_0, depends only on the structure of the porous medium. Hence, permeability is regarded as absolute regardless of the working fluid. Darcy's law defines the equation of permeability in terms of measurable quantities,[25]

$$B_0 = \frac{L \times v \times \mu}{\Delta P}$$

$$v = \frac{q}{A}$$

in which L is the length of the monolith (m), v is the linear velocity of a given fluid in the flow system (m/s), μ is the viscosity of the fluid (Pa·s), ΔP is the pressure drop when influent flows through the monolith (Pa), q is the flow rate (m^3/s), A is the cross-sectional area of the flow (m^2), and B_0 is the permeability of the porous medium (m^2).

The porosity of silica monoliths was evaluated by gravimetric measurement. The porosity was then calculated according to the following equation:

$$\text{porosity} = \left(1 - \frac{\rho_{ap}}{\rho_m}\right) \times 100\%$$

where ρ_m is the density of silica particles (ρ_m = 2.65 g/cm^3) and ρ_{ap} is the density of the prepared silica monolith.

Photocatalytic tests

The photocatalytic activity of the TiO_2 and P25 was tested by studying their effect on the decomposition of MB and MO under UV light in a batch system at room temperature. The adsorption of the TiO_2 was tested using the same method without UV light. The catalyst (20 mg) was placed in 50 mL of MB solution (10, 15, 20, and 25 mg L^{-1}) or MO solution (10 mg L^{-1}) with stirring and exposed to a UV LED lamp (λ = 365 nm, 100 mW cm^{-2}, PiPhotonics, Inc. HLKK60). Prior to the decomposition experiment, the solution with the catalyst was stirred in the dark for 30 min to ensure adsorption-desorption equilibrium. The concentration of MB was measured at different time intervals after centrifugation (14×1000 rpm, 2 min, Centrifuge MiniSpin plus, Eppendorf, Japan) using a UV-visible spectrophotometer (HITACHI, U-2810). The decrease in the intensity of the most prominent absorption band of the MB spectrum at 664 nm, and MO spectrum at 465 nm was analyzed to follow the

degradation of the dye solution. The reusability of the inorganic oxide fibers was tested by studying their effect on the decomposition of MB under UV light in a batch system at room temperature; the concentration of MB was checked at different time intervals after centrifugation using a UV-visible spectrophotometer. This experiment was repeated under identical conditions. To avoid the effect of the remaining reactants in the catalyst, the TiO_2 was washed with water and dried at 80 °C overnight before testing its recycling performance.

1.3 Results and Discussion

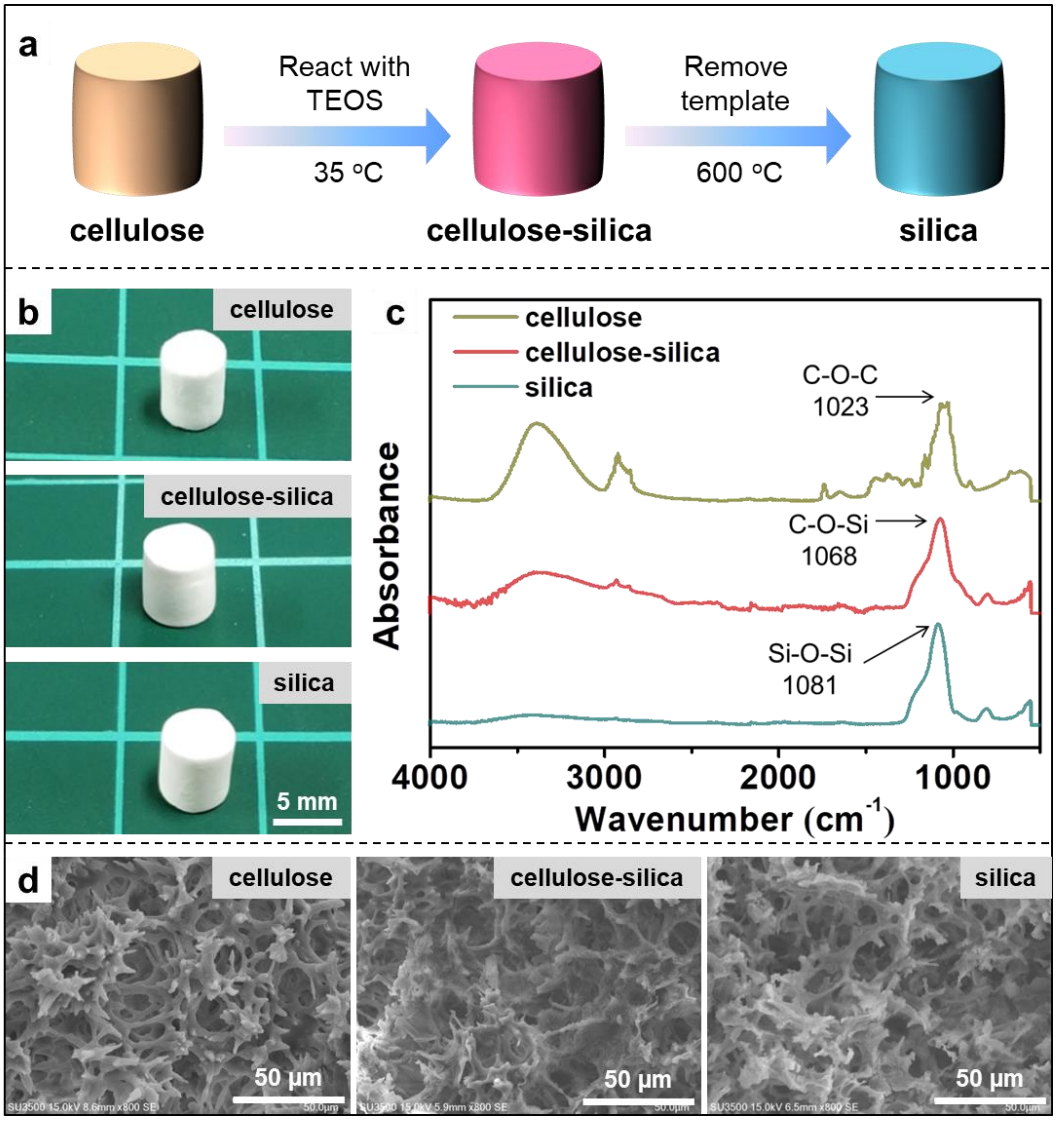

Figure 1-2 (a) Schematic illustration for preparation of silica monolith. (b) Macroscopic images, (c) FT-IR spectra, and (d) SEM images of the prepared cellulose80, cellulose80-silica50, and silica80_50 monoliths.

Figure 1-2a shows the schematic illustration for the preparation of the silica monolith using a cellulose monolith as a template. The hierarchically porous cellulose monolith was fabricated according to the TIPS method reported in a previous work.[17] First, the cellulose-silica monolith was prepared by the sol-gel method by a reaction of TEOS with the cellulose monolith. The cellulose monolith template was then removed by burning at 600 °C to obtain the silica monolith. After the sol-gel reaction, the cellulose-silica monolith remained in a good columnar shape and became larger

than the cellulose monolith. By removal of the cellulose, a silica monolith with good columnar shape was also prepared, despite a slight shrinkage compared to the cellulose-silica monolith (**Figure 1-2b**). Decomposition of cellulose was confirmed by FT-IR and TGA measurements. As shown in **Figure 1-2c**, in the FT-IR spectrum of the cellulose monolith, the bands at 1023 and ~3400 cm^{-1} are assigned to C-O-C and the stretching vibration of O-H, respectively. The cellulose-silica monolith shows a band at 1068 cm^{-1}, indicating the presence of a Si-O-C bond, while the silica monolith shows a band at 1081 cm^{-1}, indicating a Si-O-Si bond.[22] These results indicate that the prepared silica can be fixed to the cellulose template because of the condensation reaction between the hydroxyl group of cellulose and TEOS. TGA was used to study the thermal decomposition behavior of the templates from 40 °C to 800 °C. It can be seen that the weight loss of cellulose and cellulose acetate commences at 300 °C and stops after 450 °C; therefore, a burning temperature of 600 °C is enough to remove the two templates. EDS measurement showed slight residual carbon, but a white silica monolith was produced.

Porous structures of the cellulose, cellulose-silica, and silica monolith were examined *via* SEM (**Figure 1-2d**). Similar to the hierarchically porous structure of the cellulose monolith, the obtained cellulose-silica monolith and silica monolith showed a porous structure. The macropore diameter at each reaction stage was statistically analyzed based on the SEM images, the diameter of 100 pores were measured for each sample and the pore diameter were calculated, as shown in **Figure 1-3a**. The macropore diameter of the cellulose80-silica50 monolith was 21.6 ± 3.7 μm, which was smaller than that of the cellulose80 monolith (26.1 ± 4.1 μm) as a template; nevertheless, there was no significant difference after the removal of the template, which had a macropore diameter of 20.6 ± 3.1 μm.

As the TEOS concentration is considered to affect the amount of synthesized silica, the macropore diameter of the cellulose-silica and silica monoliths was evaluated as a function of TEOS concentration using the same template (cellulose80). When the TEOS concentration was under 40%, due to burning at 600 °C, the inside of the silica monolith was burned off and become a hollow structure, indicating

insufficient TEOS concentration. As shown in **Figure 1-3**, increasing the TEOS concentration tended to decrease the macropore diameter. At a TEOS concentration of 60%, the macropore diameter of cellulose-silica and silica monoliths was almost the same, but when the concentration was increased to 70%, the macropore diameter of silica was 13.7 ± 2.6 μm, which was approximately half the diameter of the cellulose monolith template. During the sol-gel reaction, a condensation reaction occurs with the hydroxyl groups of cellulose and TEOS **(Figure 1-4a**). Moreover, silica oligomers and nanoparticles are diffused into the cellulose skeleton, causing cellulose-silica to form, as shown in **Figure 1-4b**. Therefore, when the TEOS concentration is sufficiently high, the macropore diameter decreases because the amount of silica covering the skeleton surface increases.

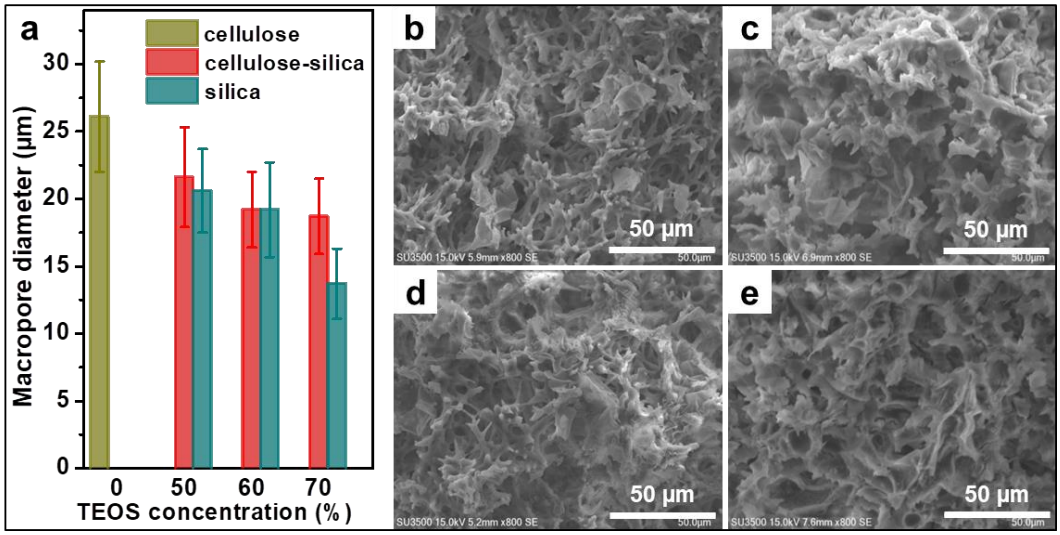

Figure 1-3 (a) Macropore diameter of cellulose, cellulose-silica, and silica monoliths prepared with different TEOS concentrations. SEM images of (b) cellulose80-silica60, (c) silica80_60, (d) cellulose80-silica70, and (e) silica80_70 monoliths.

In order to confirm the proposed mechanism, the hydrophobic cellulose acetate monolith was used as a template to prepare the silica monolith at the same reaction condition. As shown in **Figure 1-4c**, the silica precursor cannot diffuse into the hydrophobic cellulose acetate skeleton during the sol-gel process, and silica is formed on the skeleton surface and in the macropore region, although the porous structure (**Figure 1-4d**) is almost the same as the cellulose monolith (**Figure 1-2d**) because the cellulose acetate monolith is a precursor of the cellulose monolith. The cellulose

acetate-silica had a structure with voids filled by silica (**Figure 1-4e**). Consequently, the skeleton structure was not transferred, and a reversed-phase structure was obtained after template removal (**Figure 1-4f**). These results indicate that it is possible to produce a silica monolith in which the porous structure of the cellulose monolith is transferred by subjecting an appropriate concentration of TEOS to a sol-gel reaction in the presence of the cellulose monolith and subsequent removal of the template.

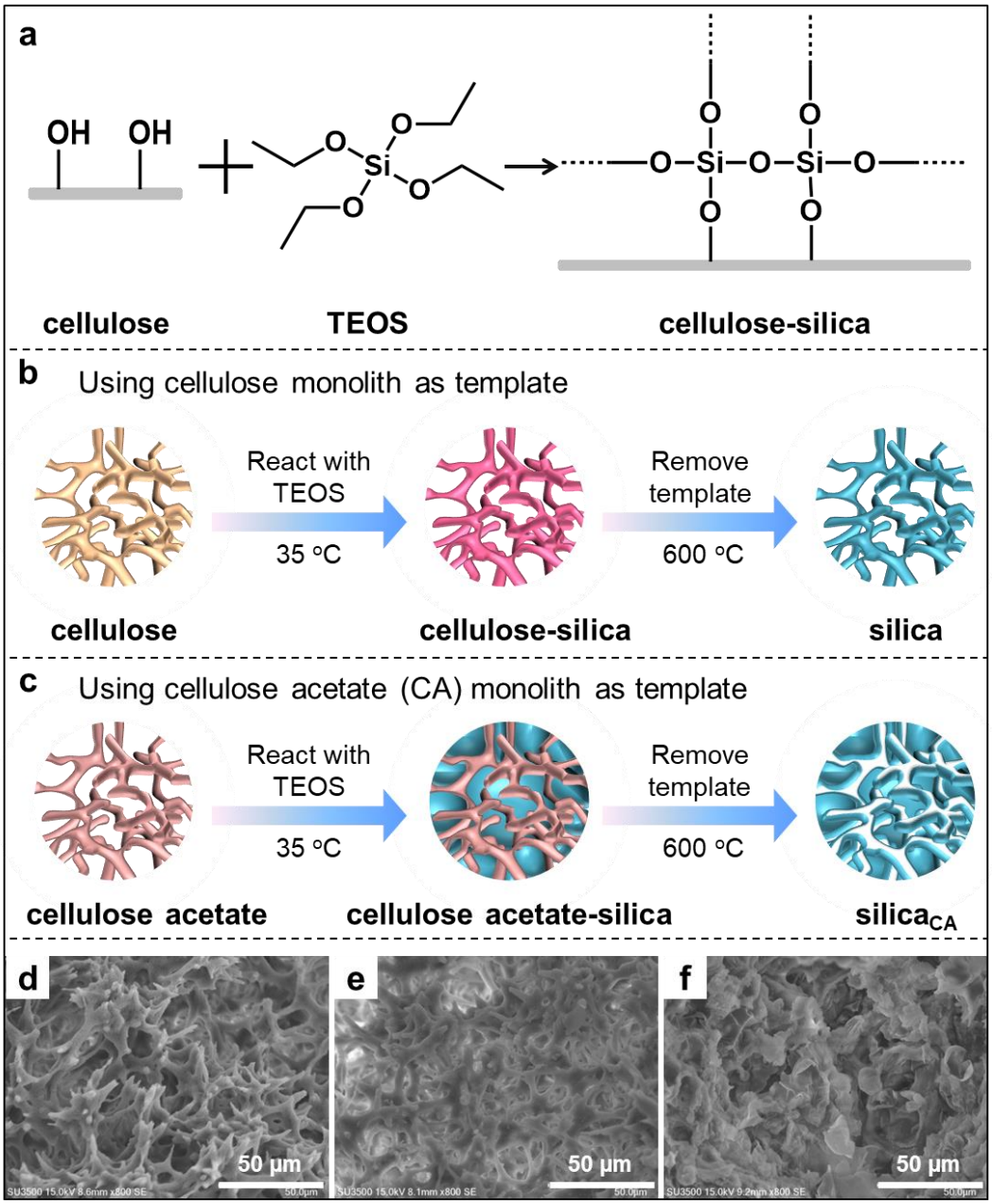

Figure 1-4 (a) Reaction between TEOS and cellulose monolith. Schematic diagram of preparation of silica monolith using (b) cellulose monolith and (c) cellulose acetate monolith as templates. SEM images of (d) cellulose acetate80, (e) cellulose acetate80-silica50, and (f) silica80CA_50 monoliths.

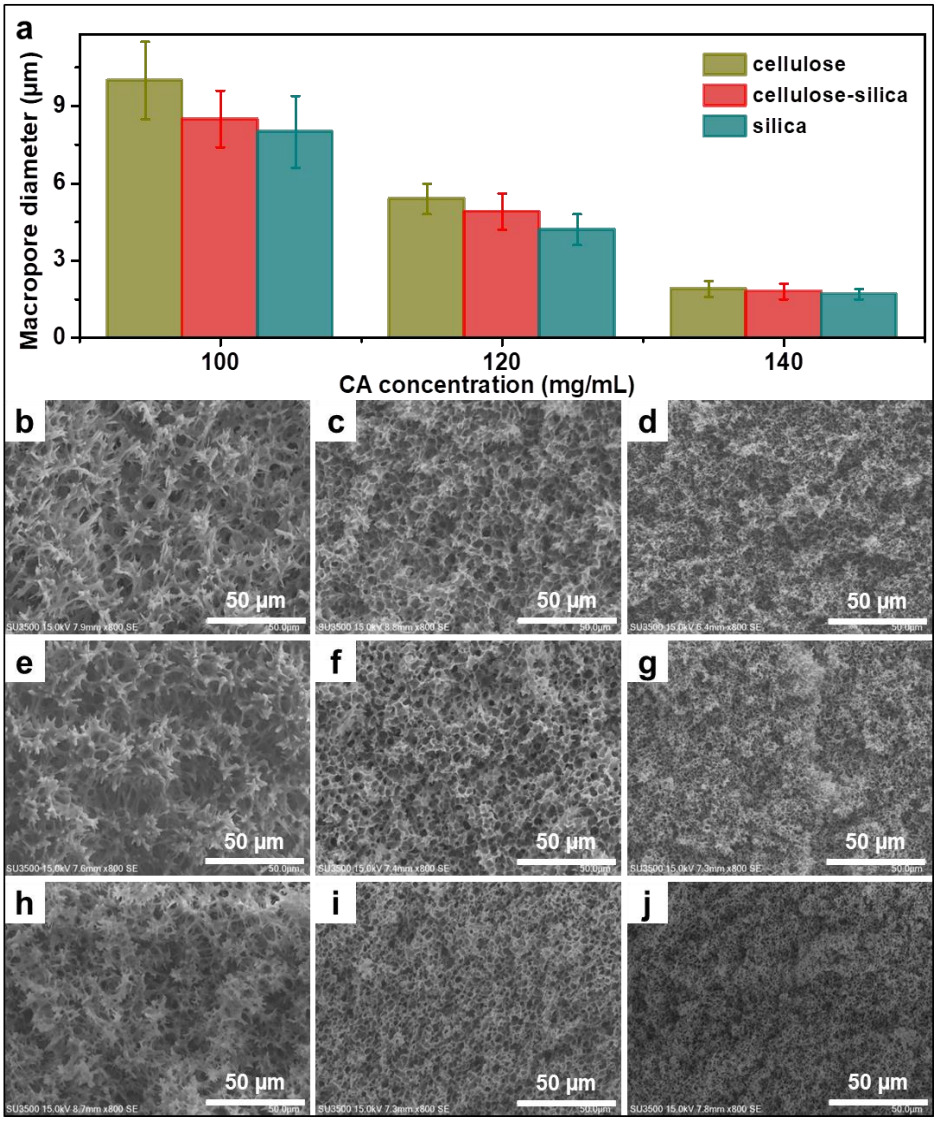

Figure 1-5 (a) Macropore diameter of cellulose, cellulose-silica, and silica monoliths prepared with different cellulose acetate concentrations. SEM images of cellulose x monolith, cellulose x-silica50, and silica x_50 monolith. x is 100 for (b), (e), and (h), 120 for (c), (f), and (i), and 140 for (d), (g), and (j).

The polymer concentration, aging temperature, and solvent composition can control the pore diameter of the cellulose monolith when the cellulose acetate monolith is a precursor of the cellulose monolith. Here, various silica monoliths with different pore diameters were prepared using a cellulose monolith template obtained when the polymer concentration was changed.[17] The concentration of TEOS was fixed at 50%. As shown in **Figure 1-3a** and **Figure 1-5a**, with the increase in cellulose acetate concentration, the macropore diameter of the cellulose monolith slightly decreased from 26.1 ± 4.1 μm (cellulose80) to 1.9 ± 0.3 μm (cellulose140),

but the obtained cellulose-silica monolith maintained the porous structure, and the silica monolith also reflected the template structure (**Figure 1-5b-j**). These results indicate that the macropore diameter of the silica monolith can be controlled by the macropore diameter of the cellulose monolith template.

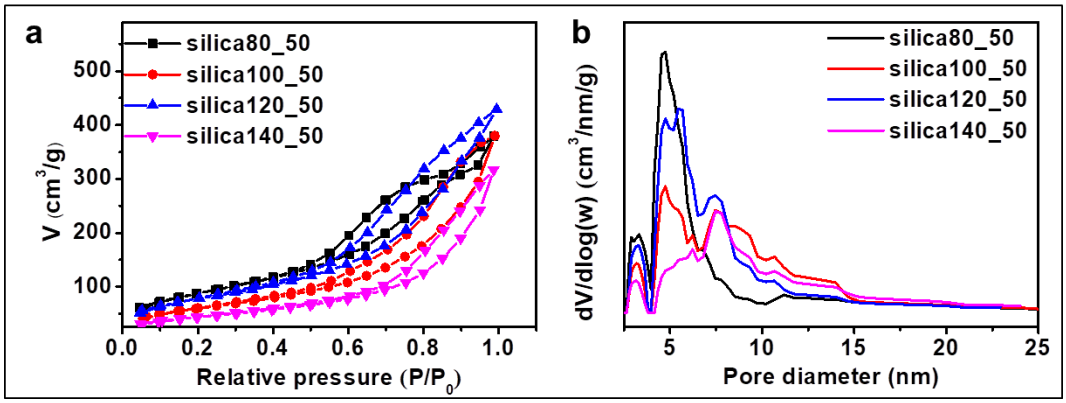

Figure 1-6 (a) Nitrogen adsorption-desorption isotherms and (b) corresponding pore size distribution curves of the silica monoliths prepared with different templates.

Table 1-1. BET surface areas, pore volumes, mean pore sizes, permeability, and porosity of silica monoliths

Sample	BET surface area (m^2/g)	Pore width (nm)	Pore volume (cm^3/g)	B_0 (m^2)	Porosity (%)
silica80_50	320	4.8	0.52	5.6×10^{-12}	86.8
silica80_60	261	5.7	0.52	9.3×10^{-12}	86.4
silica80_70	267	5.7	0.52	2.8×10^{-12}	86.8
silica100_50	261	4.8	0.55	1.7×10^{-13}	88.6
silica120_50	280	5.4	0.59	9.9×10^{-13}	89.1
silica140_50	157	7.5	0.43	4.7×10^{-13}	90.8

To evaluate the porous features of the silica monolith, nitrogen adsorption-desorption analysis was carried out; the isotherms and pore size distribution plots are shown in **Figure 1-6**. As shown in **Figure 1-6a**, all curves can be classified as type IV with adsorption hysteresis loops in terms of IUPAC classification, manifesting the presence of mesopores.[26] The BET surface area, pore volume, and pore width are summarized in **Table 1-1**. The BET surface area of the silica monolith drastically decreased from 320 m^2/g (silica80_50) to 267 m^2/g (silica80_70) with the increase in TEOS concentration, indicating that some pores are closed with a higher TEOS concentration. Additionally, the surface area slightly decreased from 320 m^2/g

(silica80_50) to 157 m^2/g (silica140_50) with the increase in cellulose acetate concentration. On the contrary, the mesopore diameter of the silica monolith increased with increasing TEOS concentration and cellulose acetate concentration, whereas the pore volume remained almost constant at 0.5 cm^3/g (**Figure 1-6b, Table 1-1**). Based on the pore diameter information obtained from nitrogen adsorption-desorption analyses and SEM observations, the silica monoliths have a broad pore diameter distribution (abundant mesopores and macropores). Moreover, due to the well-formed porous structure, the silica80_*y* monolith prepared with different TEOS concentrations possesses a similar and high porosity of 86%. With the increase in cellulose acetate concentration, the porosity of the silica *x*_50 monolith increased from 86% to 90% (**Table 1-1**).

For application as a column, liquid permeability of the solvent is required. Additionally, the absolute permeability was examined to determine the intensive property of the monolith in the flow system. The permeability coefficient in the flow system, B_0, was measured with a flow rate of 1, 2, 3, 4, and 5 mL/min, and then calculated using the average value. As shown in **Table 1-1**, the permeability varied depending on the template. The silica monolith prepared using a template with smaller macropores reduced the permeability by one order.

Silica monoliths are usually used in CO_2 capture[27] and separation[28] columns after surface modification with silane coupling agents. Therefore, surface modification of the prepared silica monolith was performed with APTMS as a model experiment (**Figure 1-7a**). No significant difference was found in the skeleton structure before (**Figure 1-7b**) and after (**Figure 1-7c**) the silane coupling reaction, but EDS measurements confirmed that nitrogen could be introduced into the silica surface. Therefore, it was clear that the present silica monolith had almost the same surface as ordinary silica, indicating that surface modification with various silane coupling agents was possible for several-column chromatography.

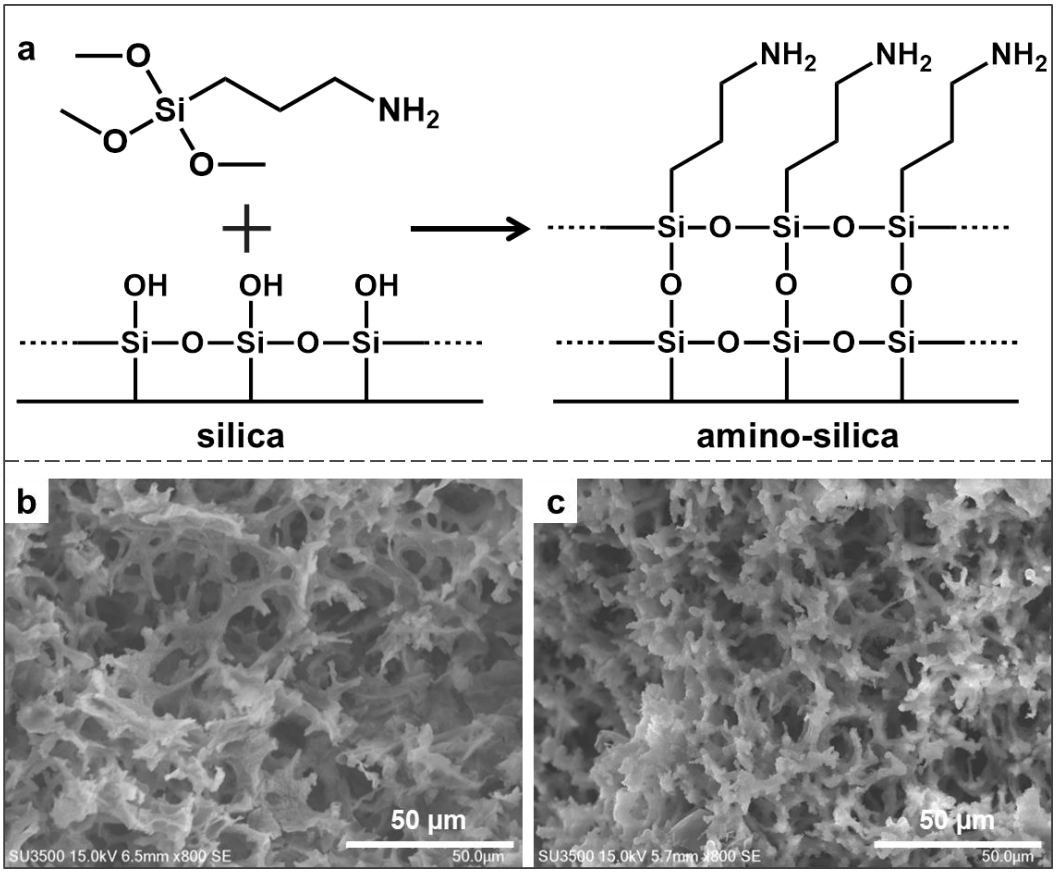

Figure 1-7 (a) Reaction mechanism of surface modification. SEM images of (b) silica80_50 and (c) amino-modified silica80_50 monoliths.

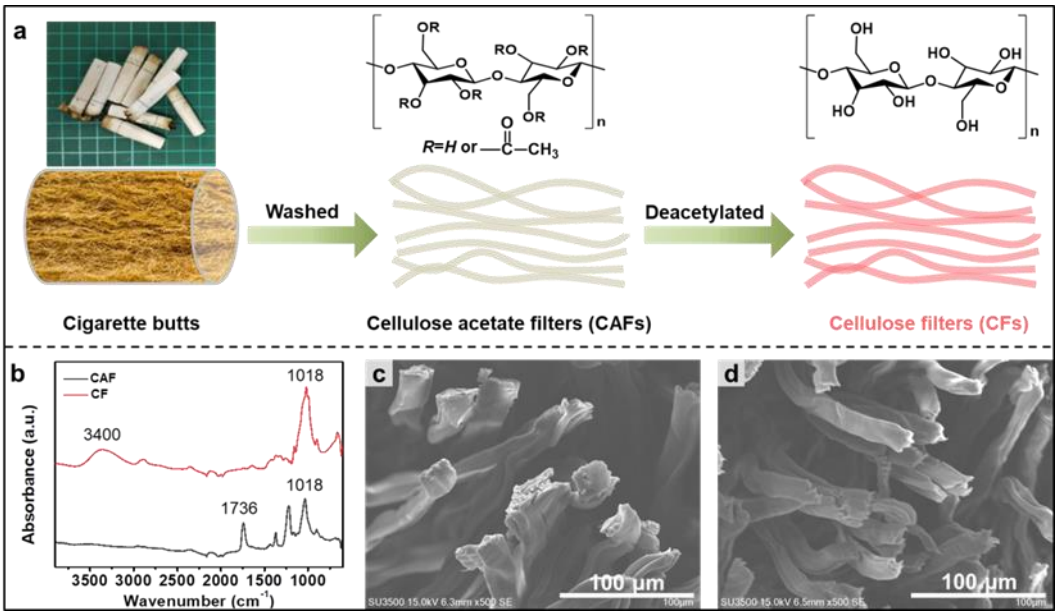

Figure 1-8 (a) The preparation process of CFs from cigarette butts. (b) FTIR spectra of the sample before and after deacetylation. SEM images of (c) CAF and (d) CF.

The used cigarette butts generally consisted of wrapping paper, remaining tobacco ash, and cellulose acetate fibers mixed together (**Figure 1-8a**). After detaching the paper and ash and repeatedly washing according to a previously reported method,[23] the obtained clean CAFs were white filters. Then, the CAF was fixed in a heat-shrinkable tube, and NaOH/methanol solution was circulated through the filter using a peristaltic pump. During this procedure, the CAF was gradually deacetylated to form CF. It should be noted that the deacetylation treatment did not destroy the structure of CAFs because this process was conducted in methanol under relatively mild conditions. To confirm the success of this reaction, the FTIR spectra of CAF and CF were measured and are compared in **Figure 1-8b**. Characteristic peaks of CAF are seen at 1018 and 1736 cm^{-1}, which can be assigned to C–O–C and C=O, respectively. The strong characteristic peak at 1736 cm^{-1} due to the stretching vibration of C=O of the acetyl group completely disappeared in the spectrum after the hydrolysis. Additionally, the broad absorbance peak at ~3400 cm^{-1} due to the stretching vibration of O-H became much larger after the hydrolysis. Meanwhile, the CF features band at 1018 cm^{-1}, which can be assigned to C–O–C.[23] The results confirm that the CAFs were hydrolyzed to CFs. The morphology of CAF and CF was examined via SEM, and **Figure 1-8c–d** shows that CAFs and CF have similar anisotropic structure.

Figure 1-9a illustrates the process for preparation of TiO_2 fiber-like materials using CF as a template. First, CF-TiO_2 was prepared by the sol-gel method by a reaction of TTIP with CF. After the sol-gel reaction, the CF-TiO_2 retained a columnar shape. The CF template was then removed by burning at 500 °C to obtain a TiO_2 fiber-like material with a good columnar shape, despite some shrinkage compared to CF-TiO_2. The prepared TiO_2 fiber-like material was brittle because it did not exhibit a network structure. Similar to the preparation of TiO_2, SiO_2 fiber-like material was prepared by using CF as a template and the sol-gel method also produced a good columnar shape that was brittle**.** The thermal decomposition behavior of the template from 40 to 800 °C was studied using TGA. The weight loss of CF, CF-TiO_2, and CF-SiO_2 commenced at 300 °C and stopped above 450 °C; however, TiO_2 and SiO_2

did not show any weight loss. Therefore, a burning temperature higher than 500 °C was sufficient to remove the CF template.

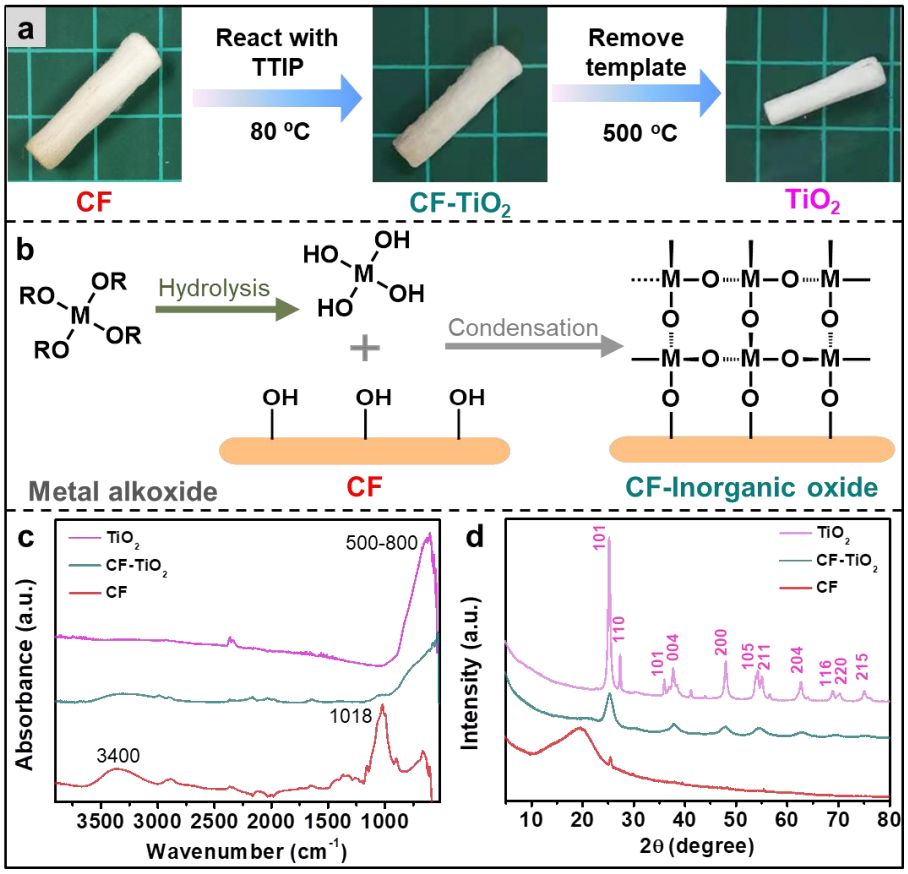

Figure 1-9 (a) The preparation process of TiO_2. (b) Reaction between metal alkoxides and CF. (c) FT-IR spectra and (d) XRD of CF, CF-TiO_2-20, and TiO_2-20.

During the sol-gel reaction, a condensation reaction occurs with the hydroxyl groups of CF and metal alkoxides (**Figure 1-9b**). The chemical structure of the samples was studied by FT-IR analysis. As shown in **Figure 1-9c**, the FT-IR spectrum of the CF features bands at 1018 and ~3400 cm^{-1}, which can be assigned to C–O–C and –OH, respectively.[29] After the sol-gel process, the peaks of the cellulose OH groups are weakened, indicating that the cellulose OH groups are bonded with TTIP. CF-TiO_2 exhibits bands at 500–800 cm^{-1}, which can be assigned to a combination of the vibrations of Ti–O–Ti and Ti–O–C bonds.[30] XRD patterns of CF, CF-TiO_2, and TiO_2 are presented in **Figure 1-9d**. The CF shows a peak consistent with the amorphous phase at 2θ = 19.7°.[31] The CF-TiO_2 has peaks at 2θ = 25.2°, 37.8°, 48.0°, 55.1°, and 62.7°, which can be indexed to the (101), (004), (200), (211), and (204) crystal faces of anatase TiO_2. TiO_2 also shows peaks consistent with the anatase phase

at 2θ = 25.2°, 37.8°, 48.0°, 54.3°, 55.1°, 62.7°, 69.0°, 70.4°, and 75.3°, which can be indexed to the (101), (004), (200), (105), (211), (204), (116), (220), and (215) crystal faces of anatase TiO_2 (PDF # 001-004-0477),[32] while the peaks located at 2θ=27.4° and 36.0° can be indexed to the (110) and (101) diffraction peaks of rutile TiO_2 (PDF # 00-001-1292). The XRD patterns of CF-SiO_2 and SiO_2 show a broad peak located at approximately 2θ=22.5°, which suggests amorphous SiO_2 (JCPDS card No. 01-086-1561) (**Figure 1-11a**).[33]

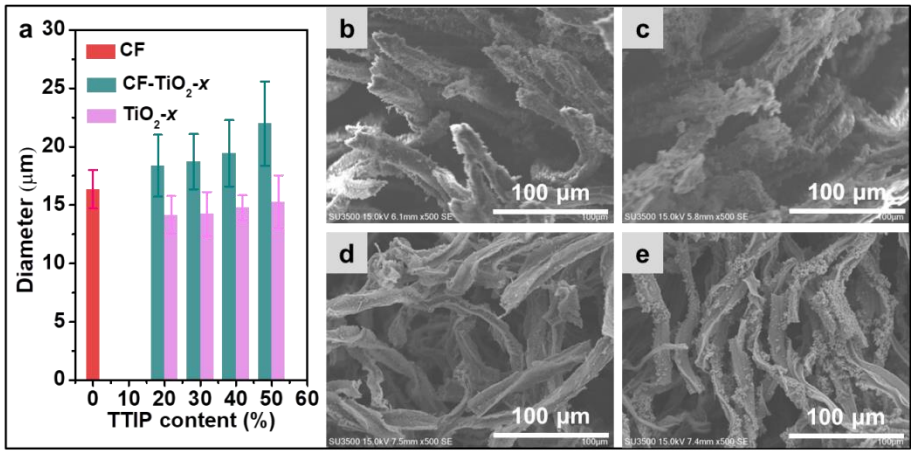

Figure 1-10 (a) Diameters of CF, CF-TiO_2, and TiO_2 fibers prepared with different TTIP contents. SEM images of (b) CF-TiO_2-20, (c) CF-TiO_2-50, (d) TiO_2-20, and (e) TiO_2-50.

The morphology of CF, CF-TiO_2, TiO_2, CF-SiO_2, and SiO_2 was examined via SEM (**Figure 1-8d, Figure 1-10, and Figure 1-11**). Similar to the fiber-like structure of the CF, the obtained CF-TiO_2, TiO_2, CF-SiO_2, and SiO_2 show fiber-like structure. The fiber diameter at each reaction stage was investigated, as shown in **Figure 1-10a** and **Figure 1-11b**. The fiber diameter of the CF-TiO_2-20 is 18.4 ± 2.6 μm, which is larger than that of the CF template (16.4 ± 1.6 μm). Furthermore, there was a significant decrease after the removal of the template, which gave a fiber diameter of 14.2 ± 1.6 μm (TiO_2-20). The fiber diameter of the CF-SiO_2-20 is 18.4 ± 2.5 μm, which is larger than that of the CF (16.4 ± 1.6 μm). Furthermore, there is a significant decrease after the removal of the template, to a fiber diameter of 16.0 ± 2.1 μm (SiO_2-20).

As the metal alkoxide content is considered to affect the amount of synthesized inorganic oxides, the diameters of CF-TiO_2, TiO_2, CF-SiO_2, and SiO_2 were evaluated

as a function of the metal alkoxide content. As shown in **Figure 1-10,** increasing the TTIP content tends to increase the diameter of the CF-TiO_2 and TiO_2. As shown in **Figure 1-11**, increasing the TEOS content tends to increase the fiber diameter of the CF-SiO_2 and SiO_2. These results indicate that with an increase in the metal alkoxide content, the diameter of the prepared inorganic oxides fibers increases because the amount of inorganic oxide covering the skeleton surface increases.

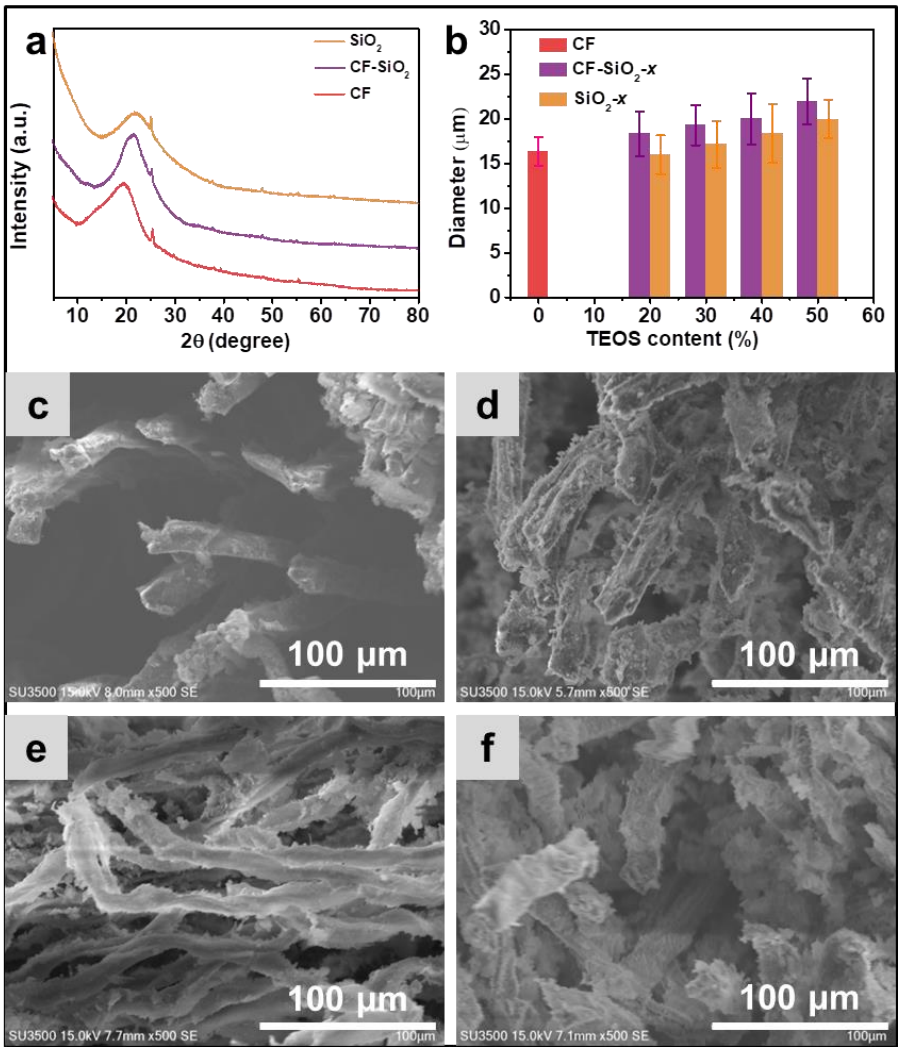

Figure 1-11 (a) XRD of CF, CF-SiO_2-20, and SiO_2-20. (b) Diameters of CF, CF-SiO_2, and SiO_2 prepared with different TEOS contents. SEM images of (c) CF-SiO_2-20, (d) CF-SiO_2-50, (e) SiO_2-20, and (f) SiO_2-50.

To evaluate the porous features of TiO_2 and SiO_2, nitrogen adsorption-desorption analysis was carried out. The isotherms and pore size distribution plots are shown in **Figure 1-12**. All curves can be classified as type IV with adsorption hysteresis loops in terms of IUPAC classification, indicating the presence of mesopores (**Figsure 1-12a** and **1-12c**).[26] The BET surface area, pore volume, and pore width are

summarized in **Table 1-2**. TiO_2-20 shows the highest surface area and pore volume (135 m^2 g^{-1}, 0.24 cm^3 g^{-1}). With an increase in TTIP content, the BET surface area and pore volume of TiO_2 decrease from 135 m^2 g^{-1} and 0.24 cm^3 g^{-1} (TiO_2-20) to 42 m^2 g^{-1} and 0.07 cm^3 g^{-1} (TiO_2-50), respectively, indicating that some pores become filled at a higher TTIP concentration. The mesopore diameters of TiO_2 were approximately 5 nm (**Figure 1-12b, Table 1-2**). Anyway, all of prepared fiber-like TiO_2 materials show higher BET surface area and pore volume than P25 (**Table 1-2**). In addition, the SiO_2-20 shows the highest surface area and pore volume (727 m^2 g^{-1}, 0.97 cm^3 g^{-1}). With an increase in TEOS content, the BET surface area and pore volume of SiO_2 decrease from 727 m^2 g^{-1} and 0.97 cm^3 g^{-1} (SiO_2-20) to 250 m^2 g^{-1} and 0.46 cm^3 g^{-1} (SiO_2-50), respectively, indicating that some pores are filled at a higher TEOS concentration. Meanwhile, the pore size distribution of SiO_2 remains mainly in the range of 2–6 nm (**Figure 1-12d, Table 1-2**).

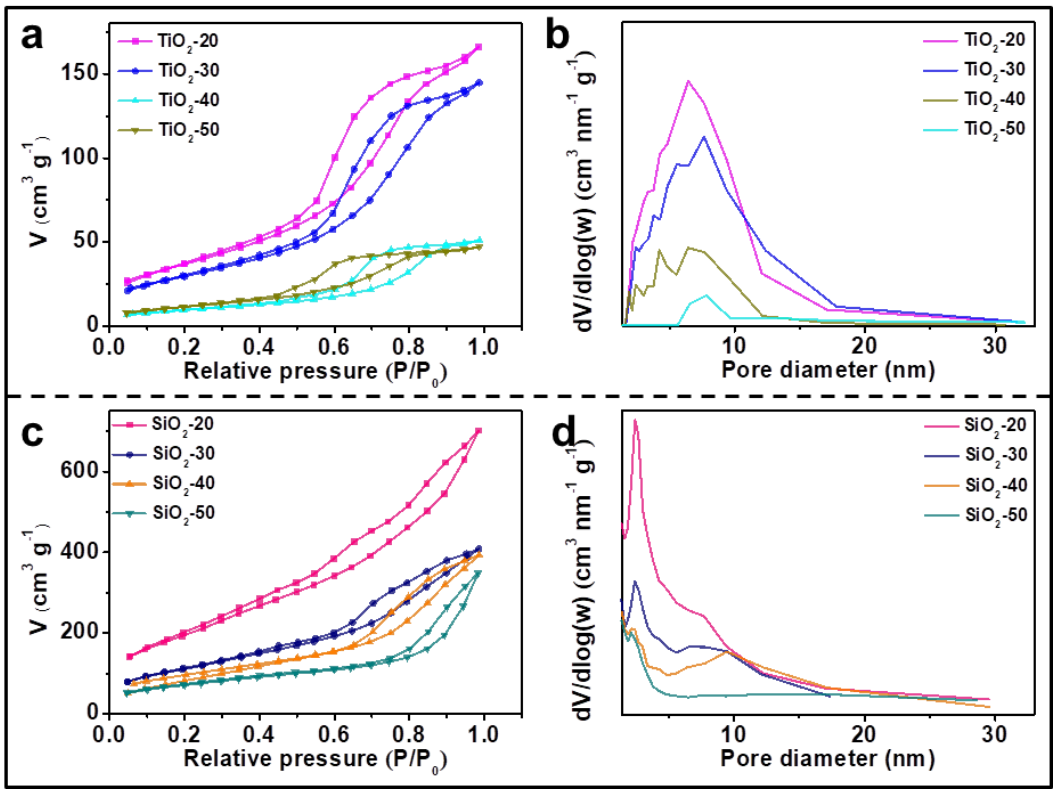

Figure 1-12 (a) Nitrogen adsorption-desorption isotherms and (b) corresponding pore size distribution curves of TiO_2 prepared with different TTIP contents. (c) Nitrogen adsorption-desorption isotherms and (d) corresponding pore size distribution curves of SiO_2 prepared with different TEOS contents.

Table 1-2. BET surface areas, mesopore diameters, and pore volumes of TiO_2 and SiO_2

Sample	Surface area (m^2 g^{-1})	Pore diameter (nm)	Pore volume (cm^3 g^{-1})
P25	7	1.9	0.02
TiO_2-20	135	6.5	0.26
TiO_2-30	108	7.7	0.23
TiO_2-40	63	7.9	0.33
TiO_2-50	42	6.5	0.08
SiO_2-20	727	2.4	1.10
SiO_2-30	404	2.4	0.64
SiO_2-40	339	1.5	0.60
SiO_2-50	250	1.4	0.54

The photocatalytic activity results are shown in **Figure 1-13**. For the tests, 20 mg of the catalyst were mixed into the MB solution (50 mL, 10 mg L^{-1}) with stirring and exposed to UV illumination (**Figure 1-13a,** inset). Control experiments were performed in the absence of a catalyst or in the presence of P25. Before photodegradation, the catalysts in the MB solution were stirred for 30 min in the dark to reach adsorption-desorption equilibrium. After 30 min, the TiO_2-20 can adsorb 3.0% of MB solution; even increase to 120 min, only 3.3% of MB solution can be adsorbed, the result shown the TiO_2-20 reached adsorption saturation after 30 min. The blank run of the samples showed approximately 6.6% MB degradation after 120 min. Under UV illumination, 94.2% of the initial dye was decomposed after 30 min, and 99.8% of the initial dye was decomposed after 120 min for P25 powders. All the results showed high MB degradation under UV irradiation. TiO_2-20 and TiO_2-30 degraded 98.4% and 97.5% of the initial dye after 30 min, respectively. They also showed better degradation efficiency than P25. TiO_2-40 and TiO_2-50 degraded 71.6% and 47.3% of the initial dye after 30 min, respectively, which was a lower degradation efficiency than P25. Nevertheless, all the samples can degrade 99% of the initial dye after 120 min, except for TiO_2-50. With an increase in TTIP content, the degradation efficiency of TiO_2 decreased, which can be attributed to the decreased surface area of the TiO_2 prepared at higher TTIP content. Owing to its high MB degradation efficiency, the stability of TiO_2-20 was evaluated through recycling experiments. As shown in **Figure 1-13b**, after five successive uses, 99.8% of the MB dye was decomposed after

120 min. **Figure 1-13c** presents the photocatalytic degradation efficiency of the TiO_2-20 under varying MB concentrations from 10 to 25 mg/L. With an increasing MB concentration, the degradation efficiency of TiO_2 shows a little decrease from 99.9 % (10 mg L^{-1}) to 97.9% (25 mg L^{-1}) after 120 min. The photocatalytic activity of TiO_2-20 for MO degradation was shown in **Figure 1-13d**, under UV illumination, 63.7% of the MO solution was decomposed after 120 min, and 99.6% of the initial dye decomposed after 300 min for TiO_2-20. These results indicate that TiO_2-20 fiber exhibited excellent photocatalytic efficiency and reusability for dye removal.

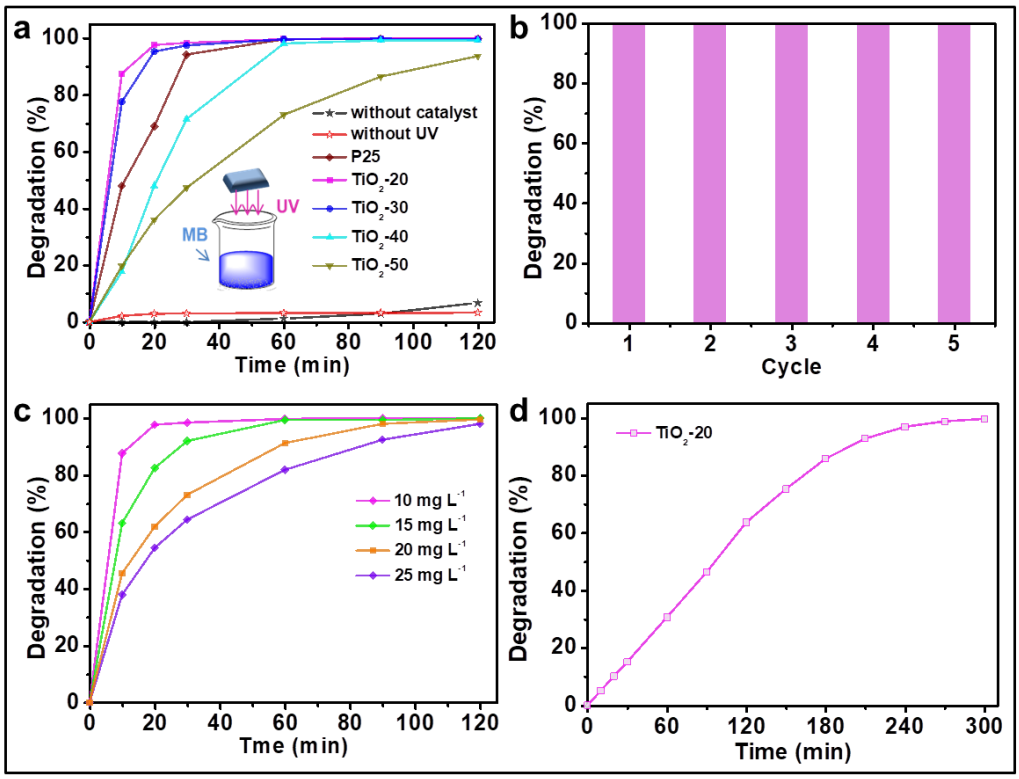

Figure 1-13 (a) Photocatalytic activity of TiO_2 and P25 for MB degradation (10 mg L^{-1}) (inset is schematic representation of the experimental setup used for the photocatalytic test). (b) Reusability efficiency of the TiO_2-20 after several photocatalytic cycles. (c) Photocatalytic degradation efficiency of the TiO_2-20 under varying MB concentrations from 10 to 25 mg L^{-1}. (d) Photocatalytic activity of TiO_2-20 for MO degradation (10 mg L^{-1}).

1.4 Conclusion

A hierarchically porous silica monolith was fabricated using a cellulose monolith as a template and TEOS as raw material by the sol-gel method. The pore structure was controlled by changing the fabrication parameters, such as the type of cellulose monolith and TEOS concentration. SEM and nitrogen adsorption-desorption analyses were carried out to evaluate the porous features of the silica monolith. The silica80_50 monolith had the largest surface area and smallest pore diameter. Moreover, due to the well-formed porous structure, the silica monolith possessed a similar and high porosity of 86%. An amino surface-modified silica monolith was also developed for further applications. The present template method for the preparation of a silica monolith is useful for the development of functional supports for column chromatography or flow reactions. Moreover, recycled cellulose acetate cigarette filters were deacetylated to cellulose filters and then applied as templates to prepare fiber-like inorganic oxides (TiO_2 and SiO_2). The TiO_2-20 and SiO_2-20 showed the highest surface area and pore volume. The TiO_2-20 fiber exhibited excellent photocatalytic efficiency and stability for water treatment. More importantly, this strategy could also be used to prepare other inorganic oxides fiber-like materials.

References

1. Z. S. Liu, P. Jiang, G. Huang, X. W. Yan and X. F. Li, *Anal. Chem.*, 2019, **91**, 3659-3666.

2. Y. T. Lai, T. C. Chen, Y. K. Lan, B. S. Chen, J. H. You, C. M. Yang, N. C. Lai, J. H. Wu and C. S. Chen, *ACS Catal.*, 2014, **4**, 3824-3836.

3. M. Moritz and M. Geszke-Moritz, *Appl. Surf. Sci.*, 2015, **356**, 1327-1340.

4. N. Gargiulo, A. Verlotta, A. Peluso, P. Aprea and D. Caputo, *Microporous Mesoporous Mater.*, 2015, **215**, 1-7.

5. C. W. Zhang, C. Z. Wang, R. Tao and J. Z. Ye, *J. Chromatogr. A*, 2019, **1590**, 58-64.

6. T. M. Budnyak, I. V. Pylypchuk, V. A. Tertykh, E. S. Yanovska and D. Kolodynska, *Nanoscale Res. Lett.*, 2015, **10**, 87.

7. A. Pipattanawarothai, C. Suksai, K. Srisook and T. Trakulsujaritchok, *Carbohydr. Polym.*, 2017, **178**, 190-199.

8. T. Hara, S. Futagami, S. Eeltink, W. De Malsche, G. V. Baron and G. Desmet, *Anal. Chem.*, 2016, **88**, 10158-10166.

9. X. J. Su, H. Q. Li, X. J. Lai, L. Zhang, J. Wang, X. F. Liao and X. R. Zeng, *ACS Appl. Mater. Interfaces*, 2017, **9**, 28089-28099.

10. O. Nunez, K. Nakanishi and N. Tanaka, *J. Chromatogr. A*, 2008, **1191**, 231-252.

11. O. Yesil-Celiktas, S. Cumana and I. Smirnova, *Chem. Eng. J.*, 2013, **234**, 166-172.

12. A. Bahrami, U. Simon, N. Soltani, S. Zavareh, J. Schmidt, M. I. Pech-Canul and A. Gurlo, *Green Chem.*, 2017, **19**, 188-195.

13. K. Nakanishi, H. Shikata, N. Ishizuka, N. Koheiya and N. Soga, *J. High Resol. Chromatogr.*, 2000, **23**, 106-110.

14. M. T. Alotaibi, M. J. Taylor, D. Liu, S. K. Beaumont and G. Kyriakou, *Surf Sci*, 2016, **646**, 179-185.

15. M. V. Santos, E. Pecoraro, S. H. Santagneli, A. L. Moura, M. Cavicchioli, V. Jerez, L. A. Rocha, L. F. C. de Oliveira, A. S. L. Gomes, C. B. de Araujo and S. J. L. Ribeiro, *J. Mater. Chem. C*, 2018, **6**, 2712-2723.

16. Z. T. Xie, T. A. Asoh and H. Uyama, *Carbohydr. Polym.*, 2019, **214**, 195-203.

17. Y. R. Xin, Q. C. Xiong, Q. H. Bai, M. Miyamoto, C. Li, Y. H. Shen and H. Uyama, *Carbohydr. Polym.*, 2017, **157**, 429-437.

18. F. L. Huang, Y. F. Xu, B. Peng, Y. F. Su, F. Jiang, Y. L. Hsieh and Q. F. Wei, *ACS*

Sustain. Chem. Eng., 2015, **3**, 932-940.

19. H. Moriwaki, S. Kitajima and K. Katahira, *Waste Manage.*, 2009, **29**, 1192-1197.

20. J. Puls, S. A. Wilson and D. Holter, *J Polym Environ*, 2011, **19**, 152-165.

21. A. L. R. Green, A. Putschew and T. Nehls, *J. Hydrol.*, 2014, **519**, 3466-3474.

22. K. L. Xie, Y. H. Yu and Y. Q. Shi, *Carbohydr. Polym.*, 2009, **78**, 799-805.

23. Z. T. Xie, T. A. Asoh and H. Uyama, *J. Hazard. Mater.*, 2020, **400**, 123303.

24. J. L. Liu and R. B. Lin, *Powder Technol.*, 2013, **241**, 188-195.

25. G. W. Jackson and D. F. James, *Can. J, Chem. Eng.*, 1986, **64**, 364-374.

26. Z. Z. Li, B. Wang, X. M. Qin, Y. K. Wang, C. T. Liu, Q. Shao, N. Wang, J. X. Zhang, Z. K. Wang, C. Y. Shen and Z. H. Guo, *ACS Sustain. Chem. Eng.*, 2018, **6**, 13747-13755.

27. G. J. Zhang, P. Y. Zhao, Y. Xu, Z. X. Yang, H. Z. Cheng and Y. F. Zhang, *ACS Appl. Mater. Interfaces*, 2018, **10**, 34340-34354.

28. L. Mafra, T. Cendak, S. Schneider, P. V. Wiper, J. Pires, J. R. B. Gomes and M. L. Pinto, *Chem. Eng. J.*, 2018, **336**, 612-621.

29. D. S. Lakshmi, N. Trivedi and C. R. K. Reddy, *Carbohydr. Polym.*, 2017, **157**, 1604-1610.

30. L. P. Liu, X. N. Yang, L. Ye, D. D. Xue, M. Liu, S. R. Jia, Y. Hou, L. Q. Chu and C. Zhong, *Carbohydr. Polym.*, 2017, **174**, 1078-1086.

31. B. X. Zhang, J. Azuma and H. Uyama, *RSC Adv.*, 2015, **5**, 2900-2907.

32. Y. H. Lv, R. H. Yuan, B. Cai, B. Bahrami, A. H. Chowdhury, C. Yang, Y. H. Wu, Q. Q. Qiao, S. Z. Liu and W. H. Zhang, *Angew. Chem. Int. Ed.*, 2020, **59**, 11969-11976.

33. Y. J. Liang, J. Ouyang, H. Y. Wang, W. L. Wang, P. F. Chui and K. N. Sun, *Appl. Surf. Sci.*, 2012, **258**, 3689-3694.

Chapter 2.

Hierarchical porous TiO_2 monolith prepared using cellulose monolith as template

2.1 Introduction

A variety of chemical substances, such as dyes, detergents, pesticides, organochlorines, and aromatic hydrocarbons, enter water bodies and cause water pollution.[1, 2] Among several water remediation methods, the photocatalytic process based on the use of titanium oxide (TiO_2) materials under UV light illumination has shown great advantages in the treatment of wastewater pollutants owing to its ability to decompose almost all organic contaminants with only photoenergy.[3] Typically, the decomposition of organic contaminants in water is performed by the simple addition of TiO_2 powder or TiO_2-based materials into the contaminated water.[4, 5] TiO_2 materials can effectively bind to organic contaminants and are light-absorbing, resulting in a high rate of the photocatalytic reaction. However, the catalyst powders need to be recovered from the suspension after the reaction. Moreover, inorganic powders frequently cause secondary pollution, which has hampered their practical application. To solve these problems, TiO_2-polymer composites are potential candidates for water remediation. For example, cellulose/TiO_2 monolith,[6] and MS@TiO_2@PPy monoliths[7] were prepared as photocatalytic materials. However, polymer-based materials are limited in their applicability due to calcination at temperatures well below 200 °C and are inadequate as catalyst support for many organocatalytic reactions due to dissolving in most organic solvents. For these reasons, hierarchically porous monolithic TiO_2 materials are potential candidates for water remediation in flow system.

Hierarchically porous materials have already received much attention in biomedical and environmental applications owing to their high surface area, high pore volume ratios, excellent accessibility to active sites, and enhanced mass transport and diffusion.[8-11] Compared with conventional porous materials with uniform pore

dimensions, hierarchical porous materials with well-defined pore dimensions and topologies can offer the combined benefits of each pore size in a single structure. For example, micro-/mesopores possess size or shape selectivity and high surface area for active site dispersion. The macropores act as flow-through channels and can minimize diffusive resistance to mass transport and provide easier access to the active sites.[8, 12] Therefore, hierarchical porous materials show superior properties for flow-through applications and enable fast separation without loss in efficiency and high-throughput screening.[13] Many hierarchical porous materials have been prepared and used in flow system such as cellulose acetate (CA) monolith,[14] and carboxyl multiwalled carbon nanotubes/thermoplastic polyurethane-based (cMWNTs/TPU) composite monoliths.[15]

Such novel interconnected porous TiO_2 materials with a 3D network are currently attracting wide interest owing to their excellent physicochemical properties, such as high specific surface area, high chemical, thermal stabilities, and environmental benignity. These properties enable their utilization in wide applications such as water remediation, next-generation solar cells, gas sensing, and lithium/sodium-ion batteries.[4, 16-18] Novel porous TiO_2 monoliths with controlled morphology, porosities, and architectures (especially with hierarchical porosity and mesopores in combination with macropores or micropores) are highly desirable owing to their unique structural features.

Of the numerous methods for the preparation of porous inorganic materials, amphiphilic block copolymer-assisted sol–gel methods have been confirmed to be a particularly promising approach owing to their advantageous features such as low cost, operational compatibility with ambient atmosphere, and easy one-pot processing route.[19] In the sol–gel process, the hydrolysis and condensation reactions of the organic precursors are preferentially incorporated into one of the blocks through hydrogen bonds. Accordingly, reaction conditions are selected to simultaneously form co-continuous structures, resulting in a network structure of inorganic-material skeletons with macropores.[20] Mesoporous phosphate-based glass (MPG) in the P_2O_5-CaO-Na_2O system was synthesized by using a combination of sol–gel chemistry and supramolecular templating.[21] Macroporous α-Al_2O_3 was synthesized by using

dicarboxylic acids as porogenes in the sol–gel process.[22] Pudukudy et al. prepared MgO nanoparticles supported nickel and iron catalysts via a facile sol–gel route without the assistance of any surfactants.[23] However, it is difficult to maintain a porous structure because their synthesis often involves a complicated phase separation in sol–gel reactions. The most commonly used synthetic technique for the fabrication of inorganic materials is "nanocasting" (hard templating), where a hierarchical structured polymer is used as a template, followed by carbonization of the composite and subsequent removal of the template.[24-26]

Cellulose monoliths, as a result of their monolithic and hierarchically porous structure, possess several features such as hydrophilicity, easy chemical modification, large surface area, insolubility in water and common organic solvents, and high mechanical strength.[27] Additionally, hierarchically porous cellulose monoliths exhibiting high hydrophilicity and tolerance toward common solvents can be easily fabricated from a cellulose acetate solution by thermally induced phase separation (TIPS).[28] Utilizing the hydrophilic but water-insoluble properties of cellulose monoliths, it is possible to incorporate the TiO_2 precursor into the monolith skeleton during the sol–gel reaction.

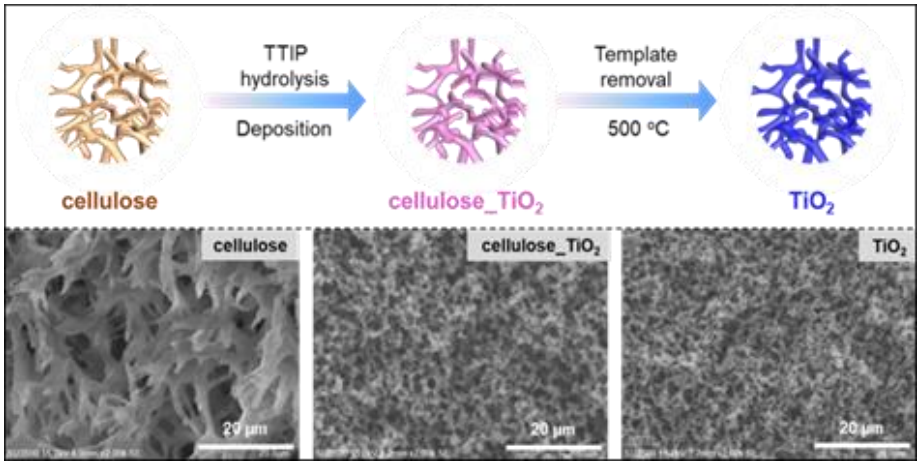

Figure 2-1 The scheme of the preparation process of TiO_2 monolith.

Herein, we used an ecofriendly cellulose monolith as a template to prepare a hierarchically porous TiO_2 monolith (**Figure 2-1**). The TiO_2 monolith was prepared in the presence of a cellulose monolith via a typical sol–gel reaction of titanium isopropoxide (TTIP). Hydrolysis and condensation reactions of TTIP occurred during

the sol–gel process. Finally, the TiO_2 monolith was obtained by heating the composite monolith in air to remove the cellulose template. Owing to the hierarchically porous structure of the cellulose monolith template, the obtained TiO_2 monolith showed a similar hierarchically porous structure. Moreover, the pore structures could be controlled by altering the fabrication parameters such as the type of cellulose monolith and TTIP content. Furthermore, the photocatalytic performance of the TiO_2 monolith was evaluated by analyzing its effect on the degradation of methylene blue (MB).

2.2 Experimental

Materials

Cellulose acetate powder (L30) with an acetylation degree of 55% was provided by Daicel Co., Ltd. Japan. TTIP (titanium (IV) isopropoxide), isopropyl alcohol, and MB were purchased from Tokyo Chemical Industry Co., Ltd. Titanium (IV) oxide (P25) was purchased from Fujifilm Wako Pure Chemical Corporation. All the other chemicals used were chemically purified and commercially purchased.

Preparation of TiO_2 monolith

The cellulose monolith was prepared via the TIPS method reported in a previous work.[28] Cellulose acetate (2.0, 2.5, 3.0, and 3.5 g) was dissolved in 10 mL of dimethylformamide (DMF) at 90 °C. Once the cellulose acetate was completely dissolved by stirring, 15 mL of 1-hexanol was added gradually. Subsequently, the mixture was continuously stirred until it became clear and then was transferred into a mold and stored at 20 ℃ for 6 h to induce phase separation, forming the cellulose acetate monolith. The dried cellulose monolith was then obtained by deacetylation under alkaline conditions (0.5 mol/L NaOH in methanol) for 3 h and vacuum drying. The cellulose monoliths prepared using different concentrations of cellulose acetate were designated as cellulose *x* monoliths, in which *x* refers the concentration of cellulose acetate.

The cellulose_TiO_2 monolith was prepared via a sol–gel reaction in the presence of a cellulose monolith. TTIP was added to isopropyl alcohol and stirred for 20 min. Then, the cellulose monolith (0.50 g) was immersed in the TTIP/isopropyl alcohol solution. Subsequently, deionized water was added to the mixture under vigorous stirring. The volume ratio of isopropyl alcohol to water was 1:10. The solution was subsequently heated to 80 °C for 5 h and cooled to room temperature, following which, the cellulose *x*_TiO_2 *y* monolith was washed with distilled water and dried at 80 °C, the total volume of the solution after added distilled water is 15 mL, the TTIP content is defined as the ratio of TTIP volume to the total volume of solution, *x* refers to the concentration of cellulose acetate (mg/mL) and *y* refers to the content of TTIP

(%).The details are shown in **Table 2-1**. To remove the cellulose monolith, the cellulose_TiO_2 monolith was burned in air (heating from room temperature to 500 °C at a rate of 1 °C/min), maintained at 500 °C for 2 h, and then cooled to room temperature to prepare the TiO_2 *x_y* monolith.

Table 2-1. Details for preparation of TiO_2 monoliths with different content of TTIP.

Sample	TTIP (mL)	Isopropyl alcohol (mL)	H_2O (mL)
TiO_2 *x*_30	4.5	0.95	9.5
TiO_2 *x*_40	6.0	0.82	8.2
TiO_2 *x*_50	7.5	0.68	6.8
TiO_2 *x*_60	9.0	0.55	5.5

Characterization

Fourier transform infrared (FT-IR) measurements of the samples were performed using a Thermo Scientific Nicolet iS5 spectrometer equipped with an iD5 ATR attachment. All spectra were acquired at a resolution of 4 cm^{-1} across 100 scans in the scan range of 4000–500 cm^{-1}. The morphology of the monoliths was investigated via scanning electron microscopy (SEM) by using a Hitachi S-3000N scanning electron microscope operated at 15 kV. The Brunauer-Emmett-Teller (BET) surface area was studied by nitrogen adsorption–desorption analysis (Quantachrome Instruments). Samples were vacuum-degassed at 70 °C for 24 h prior to measurement. The pore diameter distribution and pore volume were obtained using density functional theory (DFT). Thermogravimetric analysis (TGA) was conducted using a thermogravimetric analyzer (Hitachi, STA7200RV) in the temperature range of 40–800 °C at a heating rate of 10 °C/min under nitrogen protection. Powder X-ray diffraction (XRD) patterns were obtained using a SmartLab (Rigaku Corporation, Japan) with a Cu K-beta X-ray source and a scanning speed of 5°/min over a 2θ range of 5–80°. The generator voltage and current were 45 kV and 200 mA, respectively. The elemental compositions of the surfaces were calculated using X-ray photoelectron spectroscopy (XPS, Kratos Ultra 2). For XPS, monochromatic Al Kα was used, and the power of analysis was 75 W (wide) and 150 W (narrow). The survey and high-resolution XPS spectra were collected at fixed analyzer pass energies of 160 eV and 10 eV,

respectively. To confirm reproducibility, the measurement was performed three times for each sample. The peaks were fitted using CasaXPS Version 2.3.15 (Casa Software Ltd. Japan).

To measure the permeability of the monolith, it was tightly fitted with a heat-shrink tubing and connected to a digital quantitative tubing pump (As One, DSP-100SA) and digital pressure gauge (Krone, KDM30). The peristaltic pump was employed to allow the water to flow through the monolith. The value of the permeability coefficient, B_0, depends only on the structure of the porous medium. Hence, permeability is regarded as absolute, regardless of the working fluid. Darcy's law defines the equation of permeability in terms of measurable quantities,[29]

$$B_0 = \frac{L \times v \times \mu}{\Delta P}$$

$$v = \frac{q}{A}$$

where L is the length of the monolith (m), v is the linear velocity of a given fluid in the flow system (m/s), μ is the viscosity of the fluid (Pa·s), ΔP is the pressure drop when an influent flows through the monolith (Pa), q is the flow rate (m^3/s), A is the cross-sectional area of the flow (m^2), and B_0 is the permeability of the porous medium (m^2).

The porosity of the TiO_2 monoliths was evaluated by gravimetric measurement. The porosity was then calculated according to the following equation:

$$\text{porosity} = \left(1 - \frac{\rho_{ap}}{\rho_m}\right) \times 100\%$$

where ρ_m is the density of anatase TiO_2 particles (ρ_m = 3.895 g/cm^3), and ρ_{ap} is the density of the prepared TiO_2 monolith.

Photocatalytic tests

The photocatalytic activity of the materials has been evaluated in batch and flow systems. The photocatalytic activity of the TiO_2 powders (TiO_2 monoliths were ground into powder) and P25 powders was tested by studying their effect on the decomposition of MB under UV light in a batch system at room temperature. Monolith pieces (30 mg) and P25 powders (30 mg) were placed in 50 mL of 5 mg/L MB solution under stirring and exposed to UV light LED lamp (λ = 365 nm, 100

mW/cm^2, PiPhotonics, Inc. HLKK60). Prior to the decomposition experiment, the solution with the catalyst was stirred in the dark for 30 min to ensure adsorption–desorption equilibrium, and the concentration was checked regularly. The concentration of MB was checked at different time intervals after centrifugation (14000 rpm, 2 min, Centrifuge MiniSpin plus, Eppendorf, Japan) using a UV-visible spectrophotometer (HITACHI, U-2810)

The photocatalytic activity of the TiO_2 monoliths was tested by studying their effect on the decomposition of MB under UV light in a flow system at room temperature. For the tests, the TiO_2 monolith was fixed into a PTFE heat-shrinkable tube to construct a flow system in which a peristaltic pump (EYELA, MP-1000) was employed to allow the MB solution to flow through the monolith. The reservoir was filled with 25 mL of 5 mg/L MB solution, and the flow rate of the pump was set at 3 mL/min. Prior to the decomposition experiment, the solution was allowed to flow through the monolith in the dark for 1 h to ensure adsorption–desorption equilibrium, and the concentration was checked regularly. The decomposition was induced by a 25 W UV-LED light irradiation unit with a single peak wavelength of 365 nm (CCS Inc., EFICET-8332A). The concentration of MB was checked at different time intervals using a UV-visible spectrophotometer (HITACHI, U-2810). The decrease in the intensity of the most prominent absorption band of the MB spectra, typically at 664 nm, was analyzed to follow the degradation of the MB solution. After one cycle, the TiO_2 monolith was washed and dried to test its recycling performance. Subsequently, another photocatalytic experiment was conducted as mentioned above. This process was repeated ten times. The adsorption capacity of TiO_2 monoliths was tested by using the same method without UV light.

2.3 Results and discussion

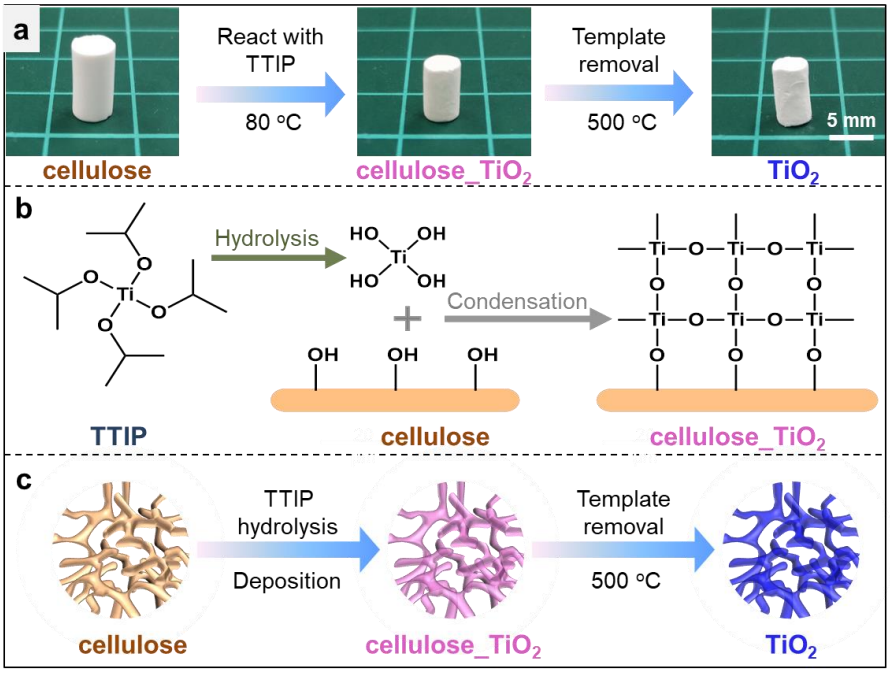

Figure 2-2 (a) The preparation process of TiO_2 monolith. (b) Reaction between TTIP and cellulose monolith. (c) Schematic diagram of preparation of TiO_2 monolith using cellulose monolith as a template.

Figure 2-2a shows a schematic illustration of the preparation of the TiO_2 monolith using a cellulose monolith as a template. The hierarchically porous cellulose monolith was fabricated according to the TIPS method reported in a previous work.[28] First, the cellulose_TiO_2 monolith was prepared via the sol–gel method and a subsequent reaction of TTIP with the cellulose monolith. After the sol–gel reaction, the cellulose_TiO_2 monolith retained a good columnar shape. The cellulose monolith template was then removed by burning at 500 °C to obtain the TiO_2 monolith. By removing the cellulose, a TiO_2 monolith with a good columnar shape was prepared. The thermal decomposition behavior of the template between 40 and 800 °C was studied by TGA (**Figure 2-3**). Usually, the decomposition temperature of a polymer under air is lower than that of under nitrogen. The weight loss of cellulose monolith under nitrogen and air commences at 300 °C and stops around 450 °C. The combustion of the cellulose produced enough energy that the temperature momentarily increased more than the programmed rate, which accounts for the

unusual shape of the curve due to the cooling that followed the reactive overheating under air. The weight loss of cellulose_TiO_2 monolith commenced at 300 °C and stopped after 450 °C; however, the TiO_2 monolith did not show any weight loss. Therefore, a burning temperature of 500 °C was sufficient to remove the template.

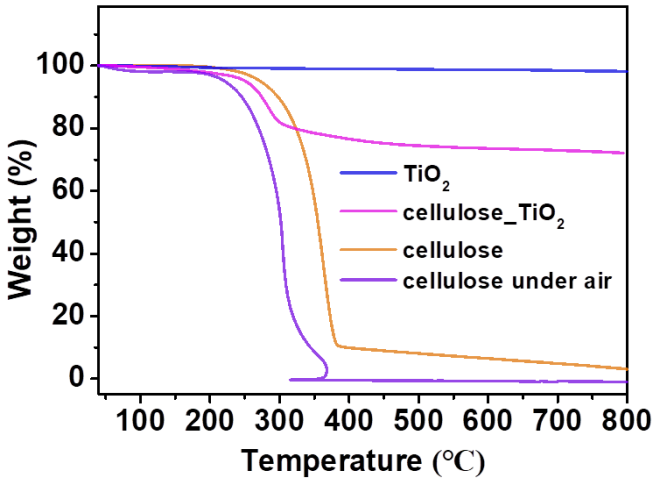

Figure 2-3 TGA measurements of cellulose, cellulose_TiO_2, and TiO_2 monoliths under nitrogen and cellulose monolith under air.

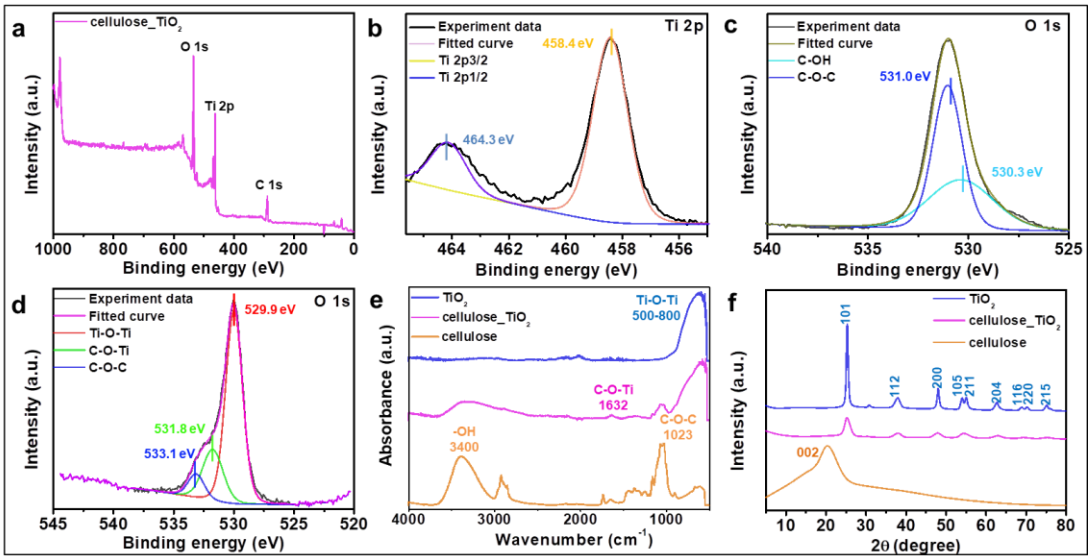

Figure 2-4 (a) Survey XPS spectra of cellulose 80 and cellulose 80_TiO_2 40. High-resolution XPS spectra of (b) Ti 2p of cellulose 80_TiO_2 40, (c) O 1s of cellulose 80 monolith, (d) O 1s of cellulose 80_TiO_2 40. (e) FT-IR spectra and (f) XRD patterns of cellulose 80, cellulose 80_TiO_2 40, and TiO_2 80_40 monoliths.

TTIP is easily hydrolyzed by H_2O molecules. The hydrolysis reaction mechanism between TTIP and H_2O molecules is an SN2 nucleophilic substitution.

During the sol–gel method, a condensation reaction also occurs between the hydroxyl groups of cellulose and TTIP (**Figure 2-2b**). In the sol–gel process, a solid substrate with hydroxyl groups on its surface is allowed to react with the metal alkoxides in solution to form covalent bonds.[30] Cellulose monoliths possess hydroxyl groups on the surface, and are suitable vehicles for the surface sol–gel process. This means that it is possible to produce a TiO_2 monolith in which the porous structure of the cellulose monolith is transferred by subjecting an appropriate quantity of TTIP to a sol–gel reaction in the presence of the cellulose monolith, followed by the subsequent removal of the template. Moreover, TiO_2 oligomers and nanoparticles diffuse into the cellulose skeleton, causing cellulose_TiO_2 to form, as shown in **Figure 2-2c**. Therefore, when the TTIP content is sufficiently high, the macropore diameter decreases because the amount of TiO_2 covering the skeleton surface increases. The chemical structure of the monolith was studied via XPS and FT-IR analyses. The XPS survey spectrum of cellulose_TiO_2 indicates the presence of Ti than pure cellulose (**Figure 2-4a**). The peaks at 458.4 and 464.3 eV are attributed to the Ti $2p_{3/2}$ and Ti $2p_{1/2}$ of TiO_2 (**Figure 2-4b**). The original cellulose monolith displayed two typical peaks at binding energies of 530.4 and 531.0 eV, corresponding to the C–OH bond and C–O–C bond of cellulose, respectively (**Figure 2-4c**). Compared with the O 1s spectrum of cellulose, the cellulose_TiO_2 has some additional characteristic signals (**Figure 2-4a**). The results obtained from the XPS analysis also suggest the presence of Ti–O–C carbonaceous bonds, which was further supported by the high-resolution O 1s XPS spectra. As shown in **Figure 2-4d**, the spectrum can be deconvoluted into three peaks: the peaks at binding energies of 529.8, 531.8, and 534.1 eV can be attributed to the Ti–O–Ti, C–O–Ti, and C–O–C bonds, respectively.[31] As shown in **Figure 2-4e**, the FT-IR spectrum of the cellulose monolith features bands at 1023 and ~3400 cm^{-1}, which can be assigned to C–O–C and –OH, respectively.[32] After the sol–gel process, cellulose_TiO_2 monoliths exhibited bands at 500–800, 1023, and 1632 cm^{-1}, indicating the presence of Ti–O–Ti, C–O–C, and C–O–Ti,[33, 34] and the TiO_2 monoliths show a band at 800–500 cm^{-1}, which can be attributed to the presence of Ti–O–Ti bonds. These results indicate that the prepared TiO_2 can be fixed to the

cellulose template because of the condensation reactions between cellulose and TTIP. XRD patterns of cellulose, cellulose_TiO_2, and TiO_2 monoliths are presented in **Figure 2-4f**. The pattern of the cellulose monolith has a peak at 2θ = 20.3°. The cellulose_TiO_2 monolith has peaks at 2θ = 25.2, 38.1, 47.9, 54.1, and 63.0°, which can be indexed to the (101), (112), (200), (105), and (204) crystal faces of anatase TiO_2. The TiO_2 monolith also shows peaks consistent with the anatase phase at 2θ = 25.2, 38.1, 47.9, 54.1, 55.1, 63.0, 69.0, 70.4, and 75.3°, which can be indexed to the (101), (112), (200), (105), (211), (204), (116), (220), and (215) crystal faces of anatase TiO_2 (PDF # 001 - 004 - 0477).[35]

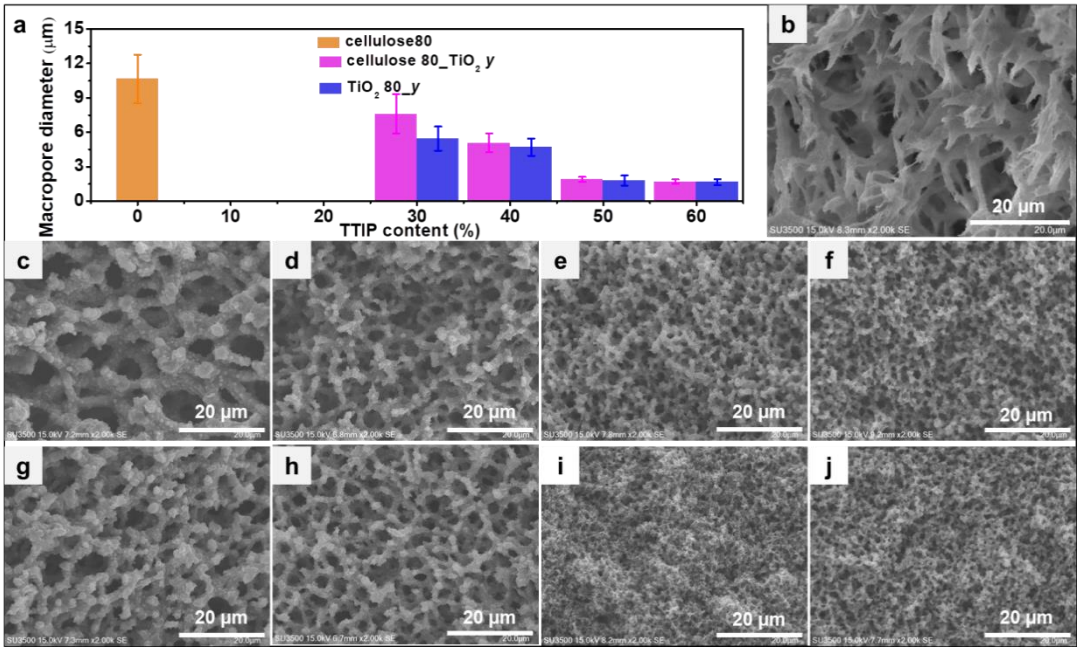

Figure 2-5 (a) Macropore diameters of cellulose, cellulose_TiO_2, and TiO_2 monoliths prepared with different TTIP contents. SEM images of (b) cellulose 80, (c) cellulose 80_TiO_2 30, (d) cellulose 80_TiO_2 40, (e) cellulose 80_TiO_2 50, (f) cellulose 80_TiO_2 60, (g) TiO_2 80_30, (h) TiO_2 80_40, (i) TiO_2 80_5, and (j) TiO_2 80_60 monoliths.

The porous structures of the cellulose, cellulose_TiO_2, and TiO_2 monoliths were examined via SEM (**Figure 2-5**). The obtained cellulose_TiO_2 and TiO_2 monoliths possessed a porous structure similar to the hierarchically porous structure of the cellulose monolith. The macropore diameters at each reaction stage were investigated, as shown in **Figure 2-5a**. The macropore diameter of the cellulose 80_TiO_2 30 monolith was 7.6 ± 1.7 μm, which was smaller than that of the cellulose 80 monolith (10.7 ± 2.1 μm) used as the template. Furthermore, the macropore diameter decreased

after the removal of the template, and the TiO_2 80_30 monolith had a macropore diameter of 5.5 ± 1.1 μm.

As the TTIP content is considered to affect the amount of TiO_2 synthesized, the macropore diameters of the cellulose 80_TiO_2 *y* and TiO_2 80_*y* monoliths were evaluated as a function of TTIP content by using the same template (cellulose 80). When the TTIP content was less than 20%, due to burning at 500 °C, the inside of the TiO_2 monolith was burned off, and it became a hollow structure. As shown in **Figure 2-5**, increasing the TTIP content tended to decrease the macropore diameters of cellulose 80_TiO_2 *y* and TiO_2 80_*y* monoliths. With a TTIP content of 40%, the macropore diameters of cellulose 80_TiO_2 40 and TiO_2 80_40 monoliths were almost similar, but when the content was increased to 60%, the macropore diameter of TiO_2 80_60 was 1.7 ± 0.3 μm, which was approximately $1/5^{th}$ of the macropore diameter of the cellulose monolith template. The results indicated that with an increase in the TTIP content, the amount of TiO_2 synthesized and attached to the surface of the cellulose monolith increased. Meanwhile, the macropore diameter of the TiO_2 80_*y* monolith decreased with an increase in the TTIP content.

When the cellulose acetate monolith is a precursor of the cellulose monolith, the pore diameter of the cellulose monolith can be controlled by adjusting the polymer concentration, aging temperature, and solvent composition.[28] In this study, various TiO_2 monoliths with different pore diameters were prepared using cellulose monolith templates obtained by varying the polymer concentration was changed when the fixed content of TTIP was 40%. As shown in **Figure 2-5a** and **Figure 2-6**, with the increase in cellulose acetate concentration, the macropore diameter of the cellulose monolith decreased slightly from 10.7 ± 2.1 μm (cellulose 80) to 1.7 ± 0.2 μm (cellulose 140), but the obtained cellulose *x*_ TiO_2 40 monoliths maintained the porous structure, and the TiO_2 *x*_40 monoliths also reflected the template structure (**Figure 2-6b–j**). These results indicate that the macropore diameter of the TiO_2 monolith can be controlled by controlling the macropore diameter of the cellulose monolith template.

To evaluate the porous features of the TiO_2 monolith, nitrogen adsorption–desorption analysis was carried out; the isotherms and pore size distribution plots are

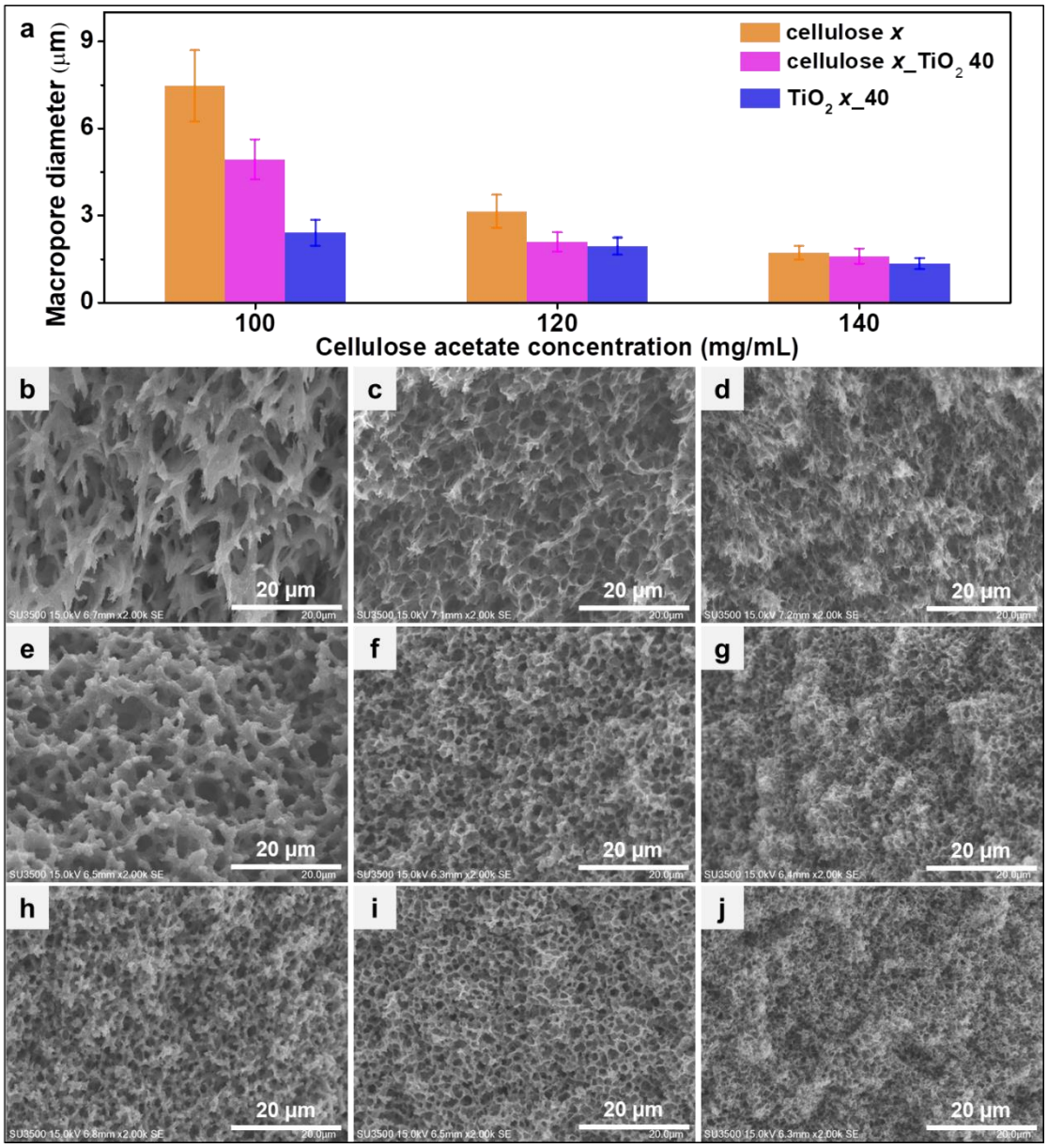

Figure 2-6 (a) Macropore diameters of cellulose, cellulose_TiO_2, and TiO_2 monoliths prepared with different cellulose acetate concentrations. SEM images of cellulose x monolith, cellulose x_ TiO_2 40, and TiO_2 x_40 monoliths. x is 100 for (b), (e), and (h); 120 for (c), (f), and (i); and 140 for (d), (g), and (j).

shown in **Figure 2-7**. As shown in **Figure 2-7a**, all the curves can be classified as type IV with adsorption hysteresis loops in terms of IUPAC classification, indicating the presence of mesopores.[36] The BET surface area, pore volume, and pore width of the TiO_2 monoliths are summarized in **Table 2-2**. The BET surface areas of all TiO_2 monoliths were similar (approximately 60 m^2/g), indicating that increasing the TTIP content or cellulose acetate concentration did not affect the surface area. Furthermore,

the mesopore diameters of the TiO_2 monoliths were 7.5 nm, except for TiO_2 80_60 (6.8 nm) and TiO_2 140_40 (7.1 nm) monoliths, whereas the pore volume remained almost constant at 0.2 cm^3/g (**Figure 2-7b, Table 2-2**). Based on the pore diameter information obtained from the nitrogen adsorption–desorption analyses and the SEM analysis, the TiO_2 monoliths have a broad pore diameter distribution (with abundant mesopores and macropores). Moreover, owing to the well-formed porous structure, the TiO_2 monoliths prepared with different contents of TTIP and cellulose acetate possessed similar and high porosities (approximately 85.9%–89.8%) (**Table 2-2**).

Table 2-2. BET surface areas, mesopore diameters, pore volumes, B_0, and porosities of TiO_2 monoliths

Sample	Surface area (m^2/g)	Mesopore diameter (nm)	Pore volume (cm^3/g)	B_0 (m^2)	Porosity (%)
TiO_2 80_30	64	7.5	0.22	1.7×10^{-11}	89.8
TiO_2 80_40	61	7.5	0.23	3.2×10^{-12}	88.8
TiO_2 80_50	60	7.5	0.24	2.2×10^{-12}	88.9
TiO_2 80_60	64	6.8	0.29	4.7×10^{-13}	87.4
TiO_2 100_40	53	7.5	0.17	1.3×10^{-13}	.87.1
TiO_2 120_40	67	7.5	0.22	2.2×10^{-13}	87.2
TiO_2 140_40	64	7.1	0.22	6.3×10^{-13}	85.9

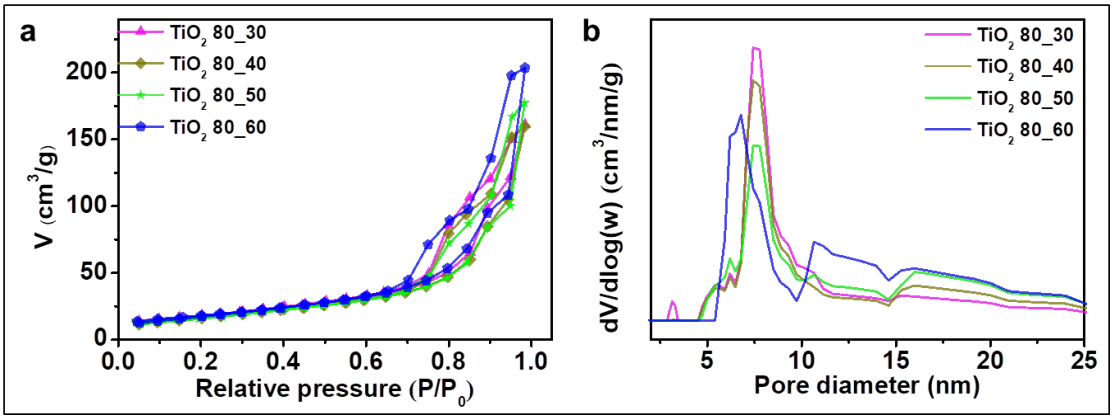

Figure 2-7 (a) Nitrogen adsorption–desorption isotherms and (b) corresponding pore size distribution curves of the TiO_2 monoliths prepared with different contents of TTIP.

For the application of these monoliths as columns, solvent permeability is required. Additionally, the absolute permeability was examined to determine the

intensive properties of the monolith in the flow system. The permeability coefficient in the flow system, B_0, was measured at a flow rate of 1, 2, 3, 4, and 5 mL/min, and then calculated using the average value. As shown in **Table 2-2**, B_0 varied depending on the TTIP content and type of cellulose monolith. B_0 decreased in the TiO_2 monolith prepared with a higher TTIP content and higher cellulose acetate concentration. Hence, all the prepared TiO_2 monoliths could be used in the flow system.

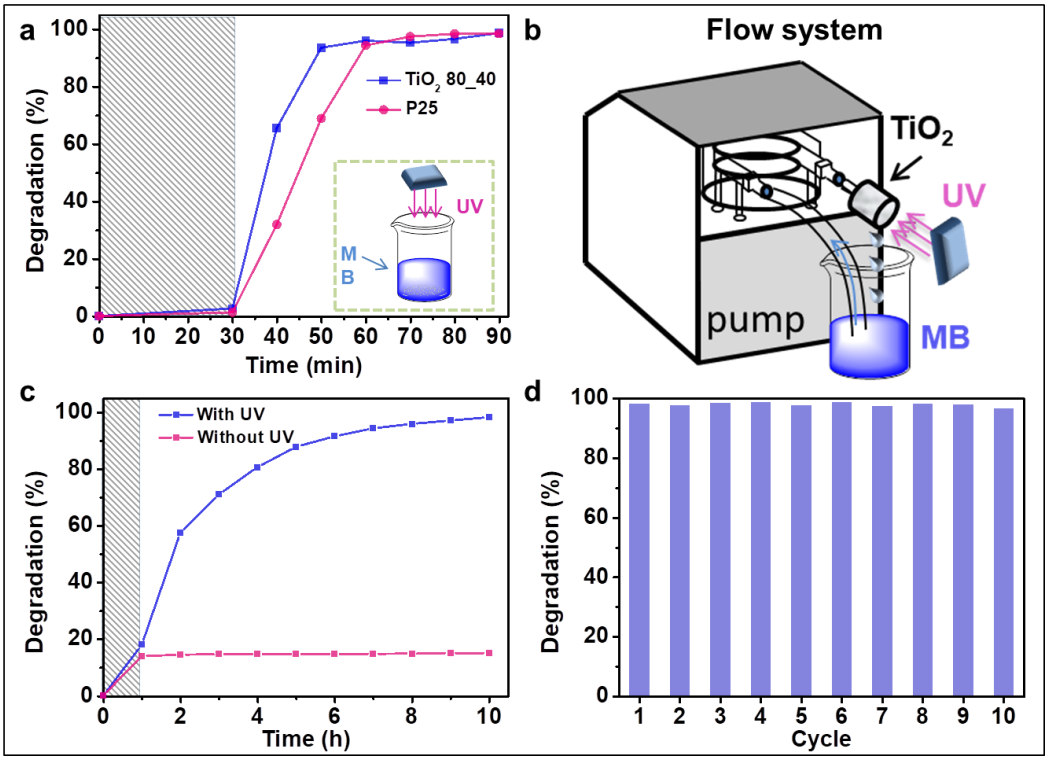

Figure 2-8 (a) Photocatalytic activity TiO_2 80_40 powder and P25 for MB solution. Shaded areas indicate periods without illumination (inset is a schematic representation of the experimental setup used for the photocatalytic test). (b) Schematic representation of the experimental setup used for the photocatalytic test at flow system. (c) Photocatalytic activity and adsorption of TiO_2 80_40 monolith for MB solution. Shaded areas indicate periods without illumination. (d) Reusability efficiency of the TiO_2 80_40 monolith after several photocatalytic cycles.

The photocatalytic activity and adsorption results are shown in **Figure 2-8**. In batch experiments, 94.5% and 96.2% of the initial dye can be decomposed after 30 min for P25 powders and TiO_2 80_40 powders under UV illumination, respectively. After 60 min, 98.6% and 98.7% of the initial dye can be decomposed for P25 powders and TiO_2 80_40 powders, respectively. The results indicate the prepared TiO_2 show

high photocatalytic activity (**Figure 2-8a**). For the flow tests, the TiO_2 80_40 monolith (φ8 × 7 mm) was fixed in a shrinkable tube and exposed to UV illumination, and the MB solution was flowed circularly through the monolith using a peristaltic pump(EYELA, MP-1000) (**Figure 2-8b**). The distance between UV light and monolith is 5 cm. After 1 h, the TiO_2 80_40 monolith can adsorb 14.1% of MB solution; even increase to 10 h, only 15.0% of MB solution can be adsorbed, the result shown the TiO_2 80_40 monolith reached adsorption saturation after 1 h. For the photocatalytic activity, 91.5% of the initial dye can be decomposed after 5 h under UV illumination. After 9 h of irradiation, 98.2% of the initial dye was decomposed (**Figure 2-8c**). The stability of the TiO_2 80_40 monolith was evaluated by recycling experiments. As shown in **Figure 2-8d**, after ten successive uses, it can decompose 96.6% of the MB dye. This indicated the good stability and reusability of the TiO_2 monolith.

2.4 Conclusions

A hierarchically porous TiO_2 monolith was fabricated via the sol–gel method by using a cellulose monolith as a template and TTIP as a raw material. The pore structures were controlled by changing the fabrication parameters, such as the type of cellulose monolith and TTIP content. SEM and nitrogen adsorption–desorption analyses were carried out to evaluate the porous features of the TiO_2 monolith. The BET surface areas of all the TiO_2 monoliths were similar, indicating that increasing the TTIP content or cellulose acetate concentrations did not affect the surface areas of the TiO_2 monolith. Moreover, owing to their well-formed porous structure, the TiO_2 monoliths possessed a high porosity (approximately 85.9%–89.8%). The TiO_2 monolith exhibited excellent photocatalytic efficiency; the degradation efficiency of MB reached 98.2%. After ten cycles, the monolith also showed a degradation efficiency of more than 96%. Therefore, the TiO_2 monolith was quite stable and reusable. We also believe that the prepared TiO_2 monoliths are promising in other application and further modification. More importantly, this strategy also can be used to prepare other inorganic monolith.

References

1. A. R. Khataee and M. B. Kasiri, *J. Mol. Catal A-chem.*, 2010, **328**, 8-26.

2. M. M. Mekonnen and A. Y. Hoekstra, *Environ. Sci. Technol.*, 2015, **49**, 12860-12868.

3. K. Nakata, T. Kagawa, M. Sakai, S. Liu, T. Ochiai, H. Sakai, T. Murakami, M. Abe and A. Fujishima, *ACS Appl. Mater. Interfaces*, 2013, **5**, 500-504.

4. Y. Y. Sheng, J. Yang, F. Wang, L. C. Liu, H. Liu, C. Yan and Z. H. Guo, *Appl. Surf. Sci.*, 2019, **465**, 154-163.

5. F. Azeez, E. Al-Hetlani, M. Arafa, Y. Abdelmonem, A. A. Nazeer, M. O. Amin and M. Madkour, *Sci. Rep.*, 2018, **8**, 7104.

6. M. A. Lucchini, E. Lizundia, S. Moser, M. Niederberger and G. Nystrom, *ACS Appl. Mater. Interfaces*, 2018, **10**, 29599-29607.

7. S. W. Yan, Y. Li, F. Xie, J. Wu, X. H. Jia, J. Yang, H. J. Song and Z. Z. Zhang, *ACS Sustain. Chem. Eng.*, 2020, **8**, 5347-5359.

8. S. Dutta, A. Bhaumik and K. C. W. Wu, *Energy Environ. Sci.*, 2014, **7**, 3574-3592.

9. J. Xiao, D. H. Mei, X. L. Li, W. Xu, D. Y. Wang, G. L. Graff, W. D. Bennett, Z. M. Nie, L. V. Saraf, I. A. Aksay, J. Liu and J. G. Zhang, *Nano Lett.*, 2011, **11**, 5071-5078.

10. Z. C. Wu, K. Tian, T. Huang, W. Hu, F. F. Xie, J. J. Wang, M. X. Su and L. Li, *ACS Appl. Mater. Interfaces*, 2018, **10**, 11108-11115.

11. T. Huang, Z. C. Wu, Q. Yu, D. G. Tan and L. Li, *Chem. Eng. J.*, 2019, **359**, 69-78.

12. Z. S. Liu, P. Jiang, G. Huang, X. W. Yan and X. F. Li, *Anal. Chem.*, 2019, **91**, 3659-3666.

13. G. Beck, M. Sieland, J. F. Beleites, R. Marschall and B. M. Smarsly, *Inorg. Chem.*, 2019, **58**, 2599-2609.

14. X. Zhang, B. Wang, X. M. Qin, S. H. Ye, Y. T. Shi, Y. Z. Feng, W. J. Han, C. T. Liu and C. Y. Shen, *Carbohydr. Polym.*, 2020, **241**, 116361.

15. S. H. Ye, B. Wang, Y. T. Shi, B. Z. Wang, Y. R. Zhang, Y. Z. Feng, W. J. Han, C. T. Liu and C. Y. Shen, *Compos. Commun.*, 2020, **21**, 100378.

16. C. X. Chu, J. Yang, Q. Q. Zhang, N. N. Wang, F. E. Niu, X. N. Xu, J. Yang, W. L. Fan and Y. T. Qian, *ACS Appl. Mater. Interfaces*, 2017, **9**, 43648-43656.

17. X. Y. Wang, J. Q. Meng, M. M. Wang, Y. Xiao, R. Liu, Y. G. Xia, Y. Yao, E. Metwalli, Q. Zhang, B. Qiu, Z. P. Liu, J. Pan, L. D. Sun, C. H. Yan, P. Muller-Buschbaum and Y. J. Cheng, *ACS Appl. Mater. Interfaces*, 2015, **7**,

24247-24255.

18. N. Hohn, S. J. Schlosser, L. BieSSmann, S. Grott, S. L. Xia, K. Wang, M. Schwartzkopf, S. V. Roth and P. Muller-Buschbaum, *Nanoscale*, 2018, **10**, 5325-5334.

19. T. M. Budnyak, I. V. Pylypchuk, V. A. Tertykh, E. S. Yanovska and D. Kolodynska, *Nanoscale Res. Lett.*, 2015, **10**, 87.

20. S. S. Yin, L. Song, S. L. Xia, Y. J. Cheng, N. Hohn, W. Chen, K. Wang, W. Cao, S. J. Hou and P. Muller-Buschbaum, *Small Methods*, 2020, **4**, 1900689.

21. F. Foroutan, B. A. Kyffin, I. Abrahams, A. Corrias, P. Gupta, E. Velliou, J. C. Knowles and D. Carta, *Acs Biomaterials Science & Engineering*, 2020, **6**, 1428-1437.

22. S. Carstens, C. Splith and D. Enke, *Sci. Rep.*, 2019, **9**, 19982.

23. M. Pudukudy, Z. Yaakob, M. Z. Mazuki, M. S. Takriff and S. S. Jahaya, *Appl. Catal. B*, 2017, **218**, 298-316.

24. S. Y. Chen, B. H. Zhou, W. L. Hu, W. Zhang, N. Yin and H. P. Wang, *Carbohydr. Polym.*, 2013, **92**, 1953-1959.

25. C. Busuioc, C. D. Ghitulica, A. Stoica, M. Stroescu, G. Voicu, V. Ionita, L. Averous and S. I. Jinga, *Ceram. Int.*, 2018, **44**, 9433-9441.

26. K. Zhou, P. Yu, X. J. Shi, T. X. Ling, W. N. Zeng, A. J. Chen, W. Yang and Z. K. Zhou, *ACS Nano*, 2019, **13**, 9595-9606.

27. Z. T. Xie, T. A. Asoh and H. Uyama, *Carbohydr. Polym.*, 2019, **214**, 195-203.

28. Y. R. Xin, Q. C. Xiong, Q. H. Bai, M. Miyamoto, C. Li, Y. H. Shen and H. Uyama, *Carbohydr. Polym.*, 2017, **157**, 429-437.

29. G. W. Jackson and D. F. James, *Can. J, Chem. Eng.*, 1986, **64**, 364-374.

30. D. H. Yu, X. D. Yu, C. H. Wang, X. C. Liu and Y. Xing, *ACS Appl. Mater. Interfaces*, 2012, **4**, 2781-2787.

31. Y. F. Sun, J. B. Zhu, L. F. Bai, Q. Y. Li, X. Zhang, W. Tong and Y. Xie, *Inorg. Chem. Front.*, 2014, **1**, 58-64.

32. D. S. Lakshmi, N. Trivedi and C. R. K. Reddy, *Carbohydr. Polym.*, 2017, **157**, 1604-1610.

33. W. B. Li, L. F. Li, X. Wu, J. Y. Li, L. Jiang, H. J. Yang, G. Z. Ke, G. Y. Cao, B. Deng and W. L. Xu, *ACS Appl. Mater. Interfaces*, 2018, **10**, 21056-21060.

34. J. Zhao, Y. Q. Gu and J. G. Huang, *Chem. Comm.*, 2011, **47**, 10551-10553.

35. Y. H. Lv, R. H. Yuan, B. Cai, B. Bahrami, A. H. Chowdhury, C. Yang, Y. H. Wu, Q. Q. Qiao, S. Z. Liu and W. H. Zhang, *Angew. Chem. Int. Ed.*, 2020, **59**, 11969-11976.

36. Z. Z. Li, B. Wang, X. M. Qin, Y. K. Wang, C. T. Liu, Q. Shao, N. Wang, J. X. Zhang,

Z. K. Wang, C. Y. Shen and Z. H. Guo, *ACS Sustain. Chem. Eng.*, 2018, **6**, 13747-13755.

Chapter 3.

A Facile Synthesis of Three-dimensional Hydroxyapatite Monolith for Protein Adsorption

3.1 Introduction

Hydroxyapatite ($Ca_{10}(PO_4)_6(OH)_2$, HA) is the main mineral component in the hard tissue of vertebrate bones and teeth as well as the most stable calcium phosphate phase under physiological conditions.[1, 2] Owing to its excellent physicochemical properties, such as biocompatibility,[3] bioactivity,[4] and osteoconductivity,[5] the synthetic HA shows promising applications in bone repair,[6] tissue engineering,[7] drug/protein/gene delivery,[8-10] and other biomedical fields.[11] However, the present HA materials show poor cell crawling and cell adhesion, slow replacement and difficult ingrowth, which limits the clinical application of HA materials.[12] One of the reasons is that they fail to provide a microenvironment suitable for bone growth, which should be a highly interconnected three-dimensional hierarchical structures with macropores and micronano structures.[13] HA-polymer composites are potential candidates to solve these problems. For example, HA/starch composites,[14] HA/cellulose,[15] and HA/cellulosetriacetate nanofibers[10] were prepared for protein adsorption and biomedical bone substitution. The improved properties of such materials result from combination of compressive strength of the inorganic ceramic phase as well as toughness and flexibility of the polymer.[16] However, there is still a high demand to discover a pure HA which can cater to unique structures and specific properties.

Hierarchically porous materials have already received much attention in biomedical and environmental applications owing to their high surface area, high pore volume ratios, excellent accessibility to active sites, and enhanced mass transport and diffusion.[17-20] Compared with conventional porous materials with uniform pore dimensions, hierarchical porous materials with well-defined pore dimensions and topologies can offer the combined benefits of each pore size in a single structure. For example, micro-/mesopores possess size or shape selectivity and high surface area for active site dispersion. The macropores act as

flow-through channels and can minimize diffusive resistance to mass transport and provide easier access to the active sites.[17, 21]

Such novel interconnected porous HA materials with a 3D network can induce early osteogenesis from the surrounding cells and tissues through cell adhesion, penetration, proliferation, and tissue ingrowth.[22] For these reasons, hierarchically porous monolithic HA materials are potential candidates for biomaterials application. A variety of methods are currently available for the preparation of hierarchical structures, such as [23], freeze-casting,[24] 3D printing.[7] Among them, sintering has the advantages of simplicity, repeatability, etc.[25] Hierarchically porous monolithic HA materials with controlled morphology, porosities, and architectures (especially with hierarchical porosity and mesopores in combination with macropores or micropores) are highly desirable owing to their unique structural features. The most commonly used synthetic technique for the fabrication of inorganic materials is hard templating, where a hierarchical structured polymer is used as a template, followed by carbonization of the composite and subsequent removal of the template.[6, 26, 27]

Cellulose monoliths, as a result of their monolithic and hierarchically porous structure, possess several features such as hydrophilicity, easy chemical modification, large surface area, insolubility in water and common organic solvents, and high mechanical strength.[28] Additionally, hierarchically porous cellulose monoliths exhibiting high hydrophilicity and tolerance toward common solvents can be easily fabricated from a cellulose acetate solution by thermally induced phase separation (TIPS).[29] Utilizing the hydrophilic but water-insoluble properties of cellulose monoliths, it is possible to incorporate the HA nanopowder into the monolith skeleton.

Herein, we used an ecofriendly cellulose monolith as a template to prepare a hierarchically porous HA monolith (**Figure 3-1**). The HA monolith was prepared in the presence of a cellulose monolith and using commercial HA powder as raw materials. Finally, the HA monolith was obtained by heating the composite monolith in air to remove the cellulose template. Owing to the hierarchically porous structure of the cellulose monolith template, the obtained HA monolith showed a similar hierarchically porous structure.

Moreover, the pore structures could be controlled by altering the fabrication parameters such as the type of cellulose monolith and HA powder content. Furthermore, the protein adsorption performance of the HA monolith was evaluated by analyzing its effect on the adsorption of bovine serum albumin (BSA).

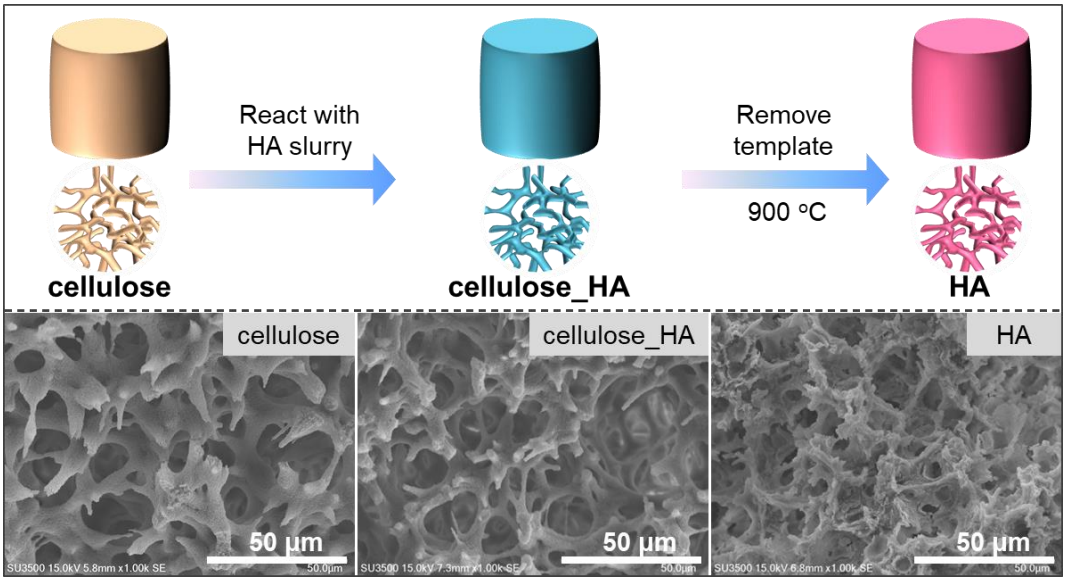

Figure 3-1 The scheme of the preparation process of hydroxyapatite (HA) monolith.

3.2 Experimental

Materials

Cellulose acetate powder (CA, L30) with an acetylation degree of 55% was kindly provided by Daicel Co., Ltd. Japan. Hydroxyapatite nanopower (<200 nm particle size (BET), ≥97%, synthetic), isopropyl alcohol and bovine serum albumin (BSA) were purchased from Sigma-Aldrich Co. LLC. Japan. Other chemicals were all chemically purified and commercially available.

Preparation of hydroxyapatite (HA) monolith

The cellulose acetate monolith and cellulose monolith were prepared *via* the TIPS method reported in a previous work. Cellulose acetate (1.75, 2.0, 2.25, 2.5, and 2.75 g) was dissolved in 10 mL of dimethylformamide (DMF) at 90 °C. When the solution was completely dissolved by stirring, 15 mL of 1-hexanol was added gradually. After continuous stirring, the mixture became clear, and was then transferred into a mold and kept at 20 °C over 6 h to induce phase separation in order to obtain the cellulose acetate monolith. The cellulose monolith was then obtained by deacetylation under alkaline conditions (0.5 mol/L NaOH in methanol) for 3 h. Finally, the dried cellulose monolith was obtained by vacuum drying. The cellulose monolith prepared with different concentrations of cellulose acetate was designated as cellulose *x* monolith, in which *x* refers to the concentration of cellulose acetate.

The cellulose_HA monolith was prepared in the presence of the cellulose monolith. First, 200 μL acetic acid was added into 10 mL of distilled water to dissolve chitosan, 0.3 g of chitosan powder was added into the aqueous acetic acid, and the mixture was kept stirring for 1 h. Then, HA powder (2, 3, and 4 g) was added into the chitosan solution slowly and kept stirring for another 2 h to obtain a homogeneous slurry. Then, cellulose monolith (0.2 g) was immersed into the HA slurry until under stirring for 48 h, the sample was washed by distilled water, following which the cellulose *x*_HA *y* monolith was obtained by drying in oven at 80 °C overnight; *x* refers to the concentration of cellulose acetate (mg/mL) and *y* refers to the amount of HA powder. For removal of the cellulose monolith, the cellulose_HA monolith was burned in air (increasing from room temperature to 900 °C at a rate of 5 °C/min), maintained

at 900 °C for 4 h, then cooled to room temperature to prepare the HA *x_y* monolith.[6]

Characterization

Fourier transform infrared (FT-IR) measurement of the samples was performed using a Thermo Scientific Nicolet iS5 spectrometer equipped with an iD5 ATR attachment. All spectra were acquired at 4 cm^{-1} resolutions over 100 scans in the scan range of 500-4000 cm^{-1}. The morphology of the monoliths was investigated by scanning electron microscopy (SEM) using a Hitachi S-3000N scanning electron microscope operated at 15 kV. The Brunauer-Emmett-Teller (BET) surface area was studied by nitrogen adsorption-desorption analysis (Quantachrome Instruments). Samples were vacuum-degassed at 70 °C for 24 h prior to measurement. The pore diameter distribution and pore volume were obtained using the density functional theory (DFT). Thermogravimetric analysis (TGA) was conducted with a thermogravimetric analyzer (Hitachi, STA7200RV) in the temperature range of 40 °C to 900 °C at a heating rate 10 °C/min under nitrogen protection. The Powder X-ray diffraction (PXRD) patterns were carried out with SmartLab (In-plane) (Rigaku Corporation, Japan) using a Cu_K-beta at a scanning speed of 5 °/min over a 2θ range of 5-80°. The generator voltage was 45 kV and the generator current was 200 mA. To measure the permeability of the monolith, it was tightly fitted with a heat shrink tubing and was then connected to a digital quantitative tubing pump (As One, DSP-100SA) and a digital pressure gauge (Krone, KDM30). The value of the permeability coefficient, B_0, depends only on the structure of the porous medium. Hence, permeability is regarded as absolute regardless of the working fluid. Darcy's law defines the equation of permeability in terms of measurable quantities,[30]

$$B_0 = \frac{L \times v \times \mu}{\Delta P}$$

$$v = \frac{q}{A}$$

in which L is the length of the monolith (m), v is the linear velocity of a given fluid in the flow system (m/s), μ is the viscosity of the fluid (Pa·s), ΔP is the pressure drop when influent flows through the monolith (Pa), q is the flow rate (m^3/s), A is the cross-sectional area of the flow (m^2), and B_0 is the permeability of the porous medium (m^2).

The porosity of HA monoliths was evaluated by gravimetric measurement. The porosity

was then calculated according to the following equation:

$$\text{porosity} = \left(1 - \frac{\rho_{ap}}{\rho_m}\right) \times 100\%$$

where ρ_m is the density of HA particles (ρ_m = 3.16 g/cm^3) and ρ_{ap} is the density of the prepared HA monolith.

Protein adsorption

BSA with an isoelectric point of 4.7 was taken as the negatively charged model protein for the present investigation. The protein adsorption capacity of the HA monoliths was tested in a flow system at room temperature. The HA monolith was fixed into a PTFE heat-shrinkable tube to construct a flow system, the protein was dissolved in 0.01M of phosphate buffer saline (PBS) solution, then the protein solution was flowed circularly through the monolith using a peristaltic pump(EYELA, MP-1000). The reservoir was filled with 20 mL of protein solution, and the flow rate was set at 2 mL/min. The concentration of protein solution was checked at different time using a UV-visible spectrophotometer (HITACHI, U-2810) at 280 nm to follow the adsorption of protein solution. The effect of pH values (BSA solution: pH 4.0–8.0, c_0 = 0.5 mg/mL) was studied. The experimental adsorption capacity for protein was calculated according to the following equation:

$$q_e = \frac{(c_0 - c_e)V}{m}$$

where q_e (mg/g) are experimental adsorption capacity for proteins, c_0 and c_e (mg/mL) are the initial and equilibrium protein concentrations, respectively; V (mL) is the volume of protein solution, and m (g) is mass of HA monolith.

3.3 Results and discussion

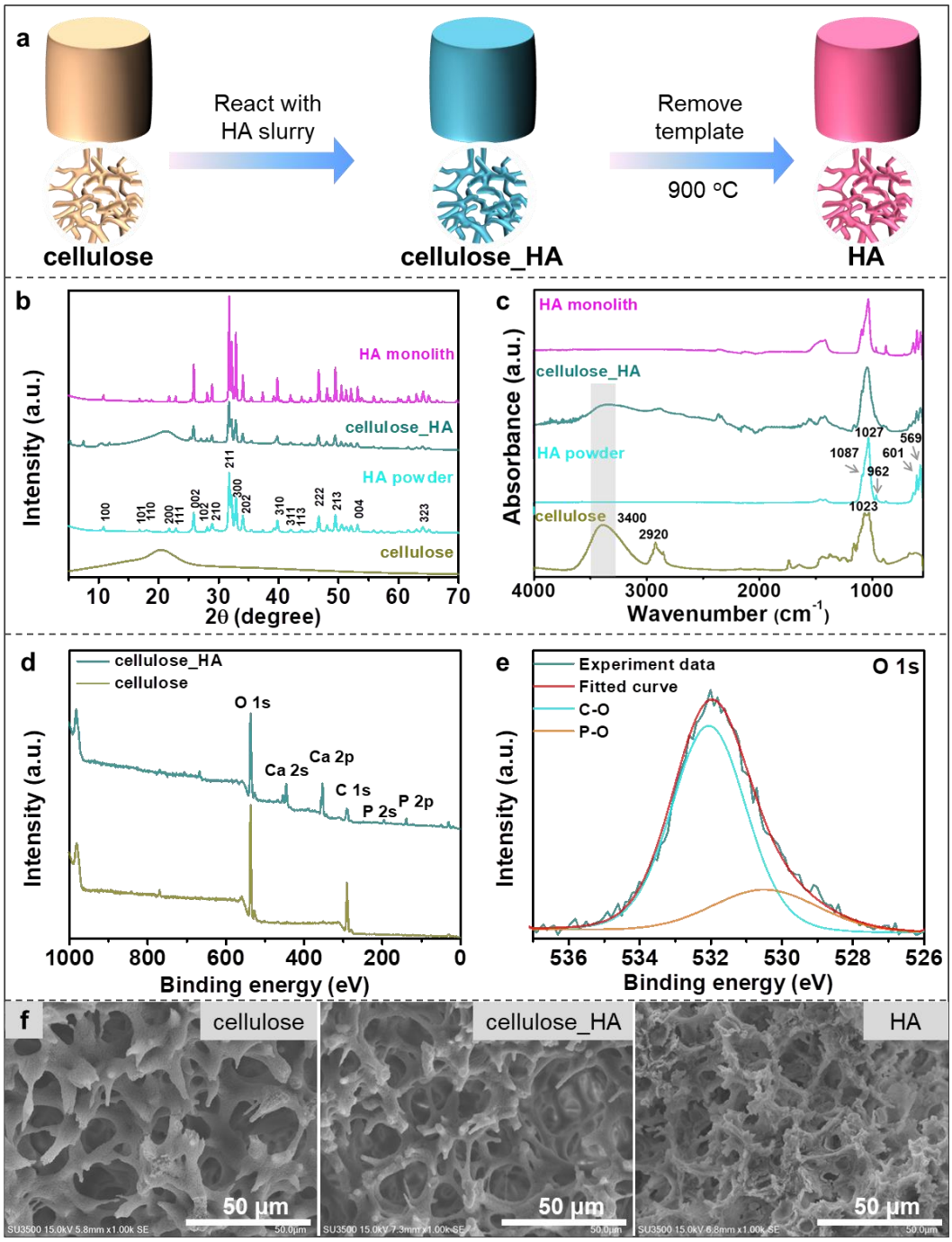

Figure 3-2 (a) Schematic illustration for preparation of HA monolith. (b) XRD spectra, (c) FT-IR spectra, (d) survey XPS spectra of cellulose 80 and cellulose80_HA2. (e) High-resolution XPS spectra of O 1s of cellulose80_HA2. SEM images of the prepared (f) cellulose80, cellulose80_HA2, and HA80_2 monoliths.

Figure 3-2a shows the schematic illustration for the preparation of the cellulose_HA monolith. The hierarchically porous cellulose monolith was fabricated according to the TIPS method reported in a previous work.[29] The cellulose_HA monolith was prepared by a reaction

of HA powder with the cellulose monolith. Then, the samples were transferred into the oven at 80 °C overnight. During drying process, with the evaporation of the solvent, water, the volume of the filled HA slurry reduced, so the vacancy uniformly appeared in the monolith. During the solvent evaporation, chitosan molecular chains shrunk. Because of the strong hydrogen bonding between chitosan molecular chains and HA powder, the shrinking of chitosan molecular chains dragged the HA and made it tightly stuck to the frame of the cellulose monolith. Thus, uniform through-hole structure was formed in the cellulose monolith. The cellulose monolith template and chitosan were then removed by burning at 900 °C to obtain the HA monolith. Simultaneously, the micropores formed on the through-hole structure because of the space occupied by HA. The thermal decomposition behavior of the template between 40 and 900 °C was studied by TGA (**Figure 3-3f**). The weight loss of cellulose and cellulose_ HA monolith commenced at 300 °C and stopped after 450 °C; therefore, a burning temperature of 900 °C was sufficient to remove the template.

The chemical structure of the monolith was studied via FT-IR, XRD and XPS analyses. XRD was further performed to characterize cellulose_HA composites, as shown in **Figure 3-2b**. The pattern of cellulose monolith has peak at $2\theta = 20.3°$, cellulose_HA monolith shows all of the peaks of cellulose and HA powder, it means that HA was successfully incorporated into cellulose monolith, after removal of template, HA monolith shows the same peaks with the HA powder. As shown in **Figure 3-2c**, in the FT-IR spectrum of the cellulose monolith, the bands at 1023, 2920 and ~3400 cm^{-1} are assigned to C-O-C, C-H and the stretching vibration of O-H, respectively. The characteristic peaks of HA powder are observed at 1027 and 962 cm^{-1} are assigned to P-O, peaks at 601 and 569 cm^{-1} are assigned to O-P-O. It can be seen that the peaks of cellulose OH groups were weaken and shifted to lower wavenumbers in the presence of HA. This result involved with intramolecular hydrogen bonding, indicating that the cellulose OH groups are bonding with HA. The formation of chemical bond between cellulose and HA can stabilize the composites. The XPS survey spectrum of cellulose_HA indicates presence of P and Ca than pure cellulose (**Figure 3-2d**). The high resolution scan XPS spectra of O 1s are shown in **Figure 3-2e**, the spectrum can be deconvoluted into two

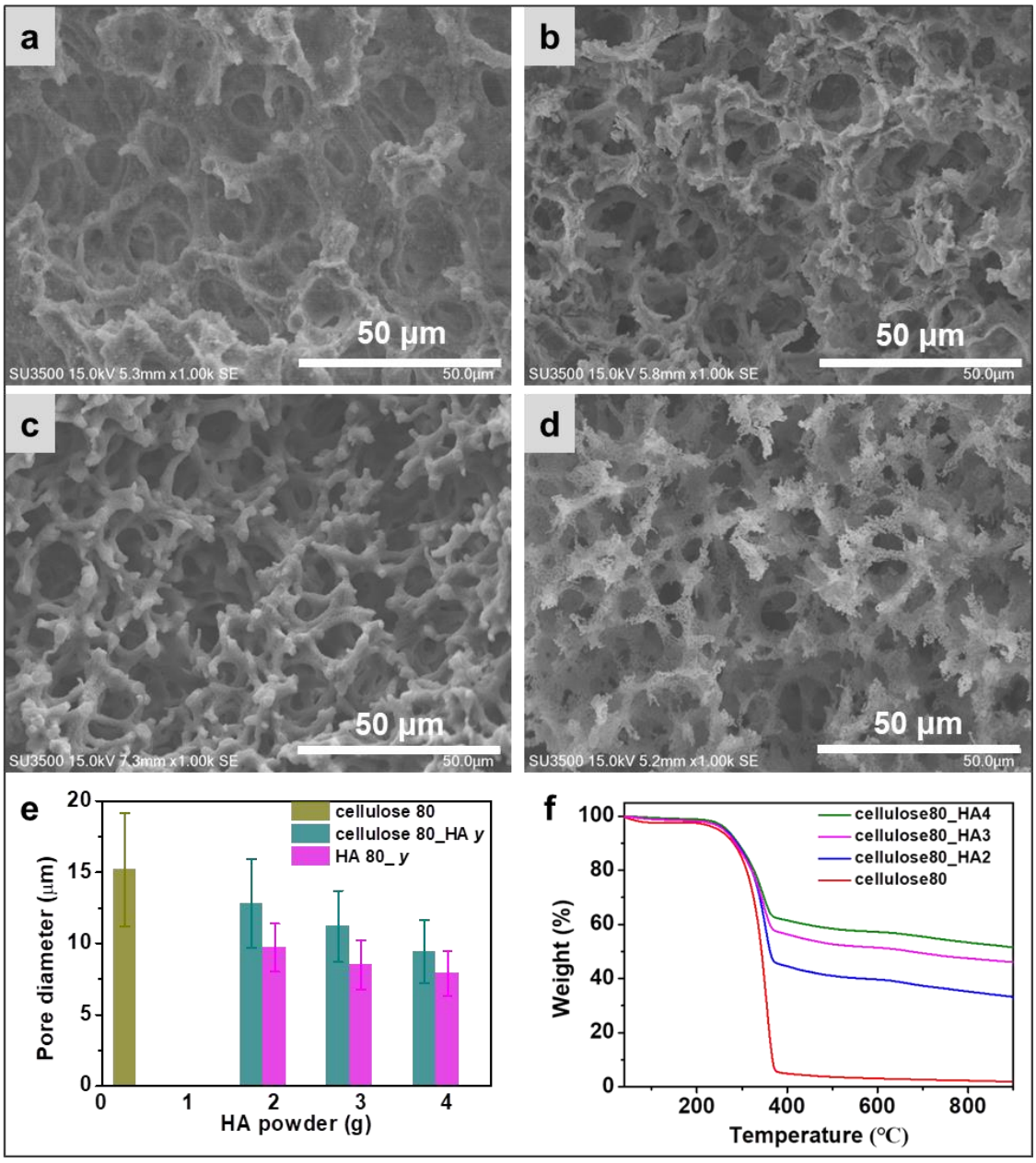

Figure 3-3 SEM images of (a) cellulose80_HA3, (b) HA80_3, (c) cellulose80_HA4, and (d) HA80_4 monoliths. (e) Macropore diameter of cellulose, cellulose_HA, and HA monoliths prepared with different amount of HA powder. (f) TGA of cellulose and cellulose_HA monoliths prepared with different amount of HA powder.

peaks: the peaks at binding energies of 530.5 and 532.0 eV can be attributed to the P–O and C–O bonds, respectively.[31]

Porous structures of the cellulose and cellulose_HA monoliths were examined *via* SEM (**Figure 3-2f**). Similar to the porous structure of the cellulose monolith, the obtained cellulose_HA and HA monoliths showed a porous structure. The macropore diameter at each reaction stage was investigated, as shown in **Figure 3-3e**. The macropore diameter of the

cellulose80_HA2 monolith was 12.8 ± 3.1 μm, which was smaller than that of the cellulose80 monolith (15.2 ± 3.9 μm) as a template; HA80_2 monolith (9.7 ± 1.7 μm) also show a smaller macropore diameter after the removal of the template.

As the amount of HA powder is considered to affect the amount of HA attached on the cellulose monolith, the macropore diameter of the cellulose_HA and HA monoliths was evaluated with different amount of HA powder using the same template (cellulose80). When the amount of HA powder was under 2 g, due to burning at 900 °C, the inside of the monolith was burned off and become a hollow structure, indicating insufficient amount of HA powder. As shown in **Figure 3-3**, increasing the amount of HA powder tended to decrease the macropore diameter. The macropore diameter at each reaction stage was investigated, as shown in **Figure 3-3e**. When the amount of HA powder is sufficiently high, the macropore diameter decreases because the amount of HA powder covering the skeleton surface increases. It also can be confirmed using TGA data, as shown in **Figure 3-3f**, with the increasing of amount of HA powder, after burning at 900 °C, the weight percent of cellulose_HA monolith was increased, it means that the amount of HA powder attached on the cellulose monolith was increased.

The polymer concentration, aging temperature, and solvent composition can control the pore diameter of the cellulose monolith when the cellulose acetate monolith is a precursor of the cellulose monolith. Here, various HA monoliths with different pore diameters were prepared using a cellulose monolith template obtained when the polymer concentration was changed.[29] The amount of HA powder was fixed at 2 g. As shown in **Figure 3-4a**, with the increase in cellulose acetate concentration, the macropore diameter of the cellulose monolith slightly decreased from 29.9 ± 7.7 μm (cellulose70) to 4.1 ± 0.7 μm (cellulose110), but the obtained cellulose_ HA monolith maintained the porous structure, and the HA monolith also reflected the template structure (**Figure 3-4b-m**). These results indicate that the macropore diameter of the HA monolith can be controlled by the macropore diameter of the cellulose monolith template.

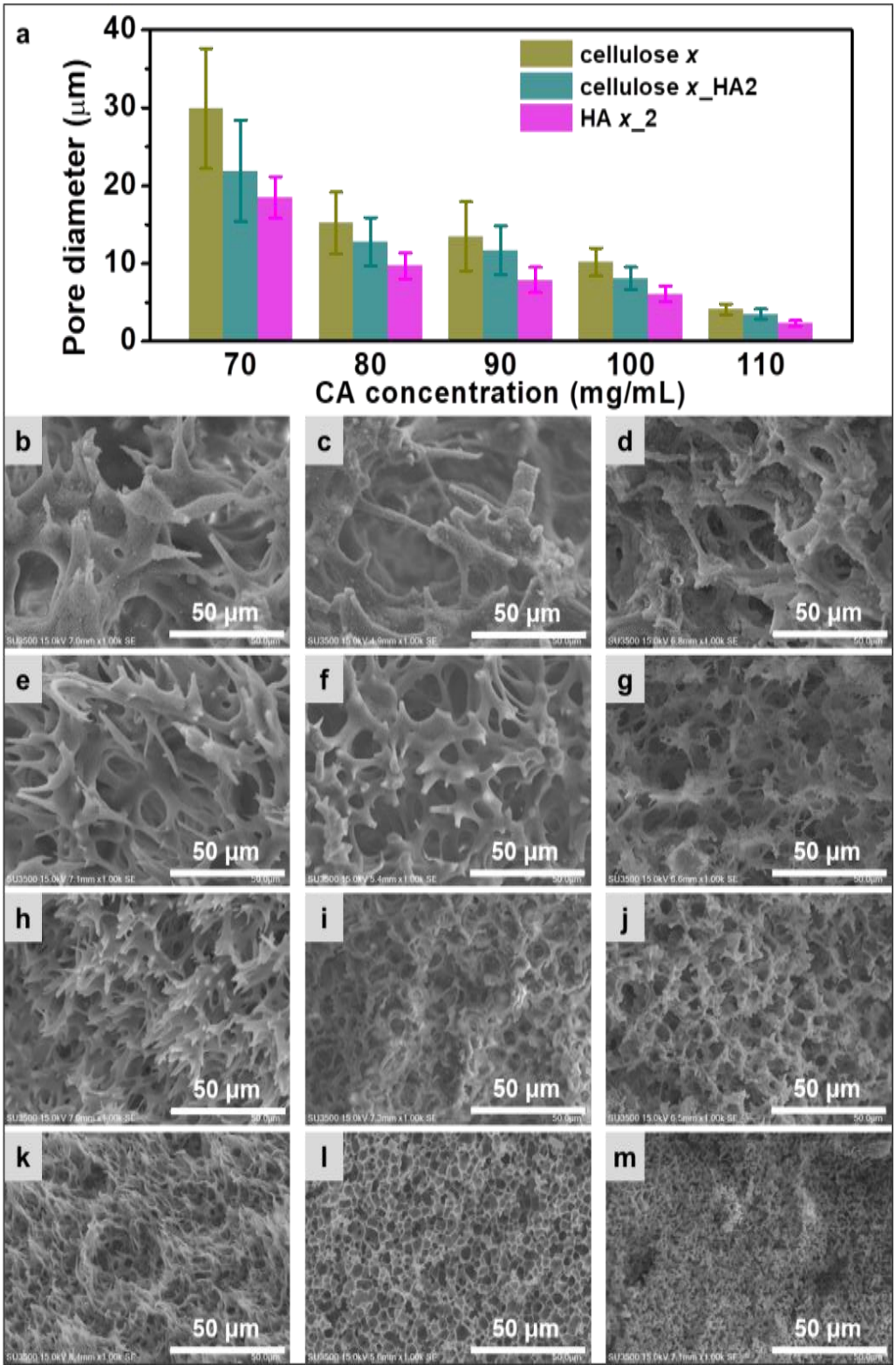

Figure 3-4 (a) Macropore diameter of cellulose, cellulose_HA, and HA monoliths prepared with different cellulose acetate concentrations. SEM images of cellulose *x* monolith, cellulose *x*_HA2, and HA *x*_2 monolith. *x* is 70 for (b), (c), and (d), 90 for (e), (f), and (g), 100 for (h), (i), and (j),and 110 for (k), (l), and (m).

To evaluate the porous features of the HA monolith, nitrogen adsorption-desorption

analysis was carried out; the isotherms and pore size distribution plots are shown in **Figure 3-5a-b**. As shown in **Figure 3-5a**, all curves can be classified as type IV with adsorption hysteresis loops in terms of IUPAC classification, manifesting the presence of mesopores. The BET surface area, pore volume, and pore width are summarized in **Table 3-1**. With the increasing of amount of HA powder or cellulose acetate concentration, HA monoliths show similar surface area, pore width and pore volume.

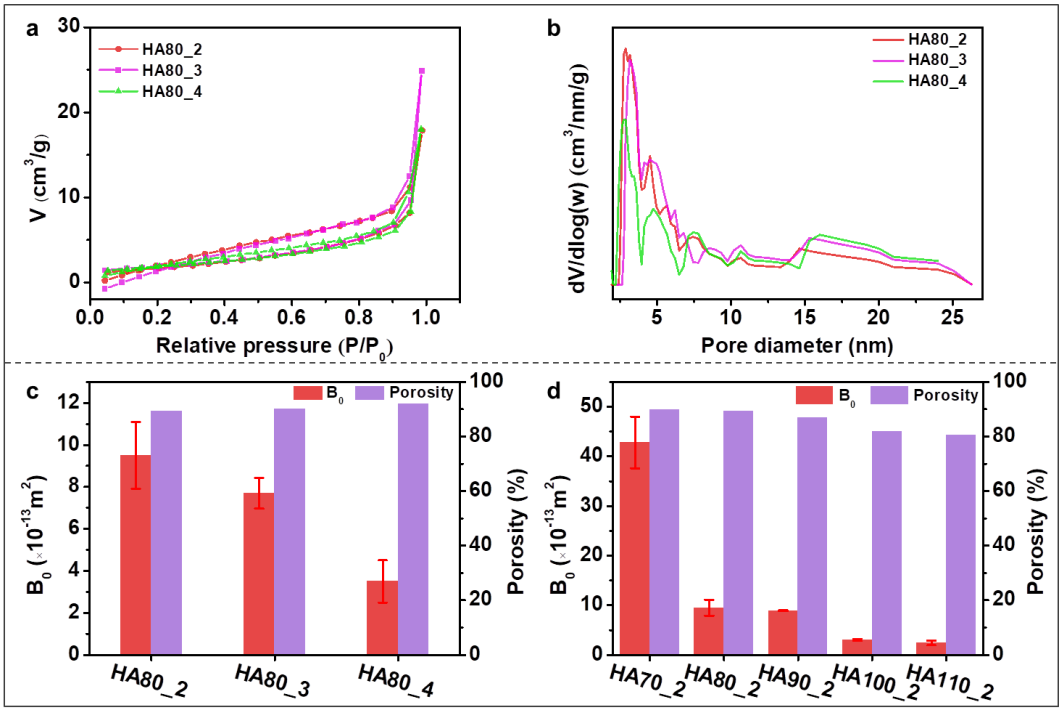

Figure 3-5 (a) Nitrogen adsorption-desorption isotherm, (b) corresponding pore size distribution curve of the HA monoliths, permeability and porosity of (c) HA80_*y* and (d) HA *x*_2 monoliths.

Table 3-1. BET surface areas, pore volumes, mesopore diameters of HA monoliths

Sample	Surface area (m^2/g)	Pore diameter (nm)	Pore volume (cm^3/g)
HA80_2	6.1	2.897	0.016
HA80_3	6.5	3.169	0.018
HA80_4	6.5	2.769	0.015
HA70_2	9.6	2.769	0.023
HA90_2	7.2	2.769	0.016
HA100_2	7.6	2.769	0.029
HA110_2	7.2	2.769	0.022

For application as a column, liquid permeability of the solvent is required. Additionally, the absolute permeability was examined to determine the intensive property of the monolith in

the flow system. As shown in **Figure 3-5c-d**, with the increasing of amount of HA powder, permeability of HA80_*y* monoliths were decreased, porosity was increased. With the increasing of CA concentration, permeability and porosity of HA *x*_2 monoliths were decreased.

HA is a well-known effective adsorbent that can adsorb positively and negatively charged proteins, DNA, biological molecules and heavy weight metal ions. Understanding the adsorption behavior of proteins is very important to found their potential impact on biomedical applications. BSA was used as a model protein for adsorption studies. The amounts of BSA adsorbed were measured by varying the pH, initial concentration of BSA, and kind of HA monolith.

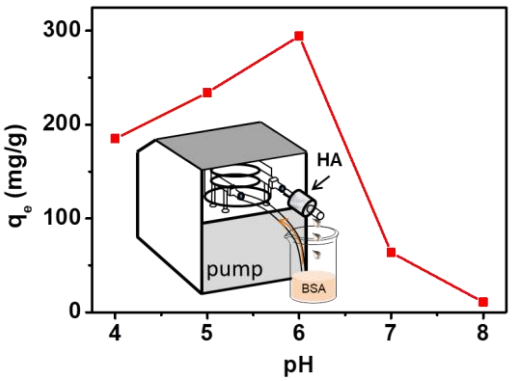

Figure 3-6 The effect of pH value of BSA (initial concentration: 0.5 mg mL-1) on the adsorption capacity for HA 80_2 monolith (inset is a schematic representation of the experimental setup used for the protein adsorption).

In general, protein adsorption is attributed to electrostatic, van der Waals and hydrophobic interactions due to the surface charges of the adsorbent. Hence, the electrostatic force of attraction between BSA and the HA monolith is the foremost function for surface adsorption. The electrostatic force is varied by altering the pH. **Figure 3-6** shows pH dependent BSA adsorption by the HA80_2 monolith in a pH range from 4.0 to 8.0 with an initial BSA concentration of 0.5 mg mL^{-1} at room temperature. It shows that a maximum BSA adsorption capacity of 294.6 mg g^{-1} occurs at pH 6.0.

3.4 Conclusions

A porous HA monolith was fabricated using a cellulose monolith as a template and commercial HA powder as raw material. The pore structure was controlled by changing cellulose acetate concentration and amount of HA powder. SEM and nitrogen adsorption-desorption analyses were carried out to evaluate the porous features of the HA monolith. Moreover, owing to their well-formed porous structure, the HA monoliths possessed a high porosity. The HA monolith exhibited excellent adsorption capacity of 294.6 mg g^{-1} for BSA adsorption. We also believe that the prepared HA monoliths are promising in other application.

References

1. L. C. Palmer, C. J. Newcomb, S. R. Kaltz, E. D. Spoerke and S. I. Stupp, *Chem. Rev.*, 2008, **108**, 4754-4783.

2. S. V. Dorozhkin, *Materials*, 2009, **2**, 399-498.

3. P. J. Shi, M. Liu, F. J. Fan, C. P. Yu, W. H. Lu and M. Du, *Mater. Sci. Eng. C*, 2018, **90**, 706-712.

4. S. Paul, A. Pal, A. R. Choudhury, S. Bodhak, V. K. Balla, A. Sinha and M. Das, *Ceram. Int.*, 2017, **43**, 15678-15684.

5. C. Shi, J. Y. Gao, M. Wang, Y. R. Shao, L. P. Wang, D. L. Wang and Y. C. Zhu, *Biomater. Sci.*, 2016, **4**, 699-710.

6. K. Zhou, P. Yu, X. J. Shi, T. X. Ling, W. N. Zeng, A. J. Chen, W. Yang and Z. K. Zhou, *ACS Nano*, 2019, **13**, 9595-9606.

7. S. C. Cox, J. A. Thornby, G. J. Gibbons, M. A. Williams and K. K. Mallick, *Mater. Sci. Eng. C*, 2015, **47**, 237-247.

8. N. K. Nga, N. T. T. Chau and P. H. Viet, *Colloids Surf. B*, 2018, **172**, 769-778.

9. Y. D. Yu, Y. J. Zhu, C. Qi and J. Wu, *Ceram. Int.*, 2017, **43**, 6511-6518.

10. T. Lan, Z. Q. Shao, J. Q. Wang and M. J. Gu, *Chem. Eng. J.*, 2015, **260**, 818-825.

11. F. Chen and Y. J. Zhu, *ACS Nano*, 2016, **10**, 11483-11495.

12. H. L. Oliveira, W. L. O. Da Rosa, C. E. Cuevas-Suarez, N. L. V. Carreno, A. F. da Silva, T. N. Guim, O. A. Dellagostin and E. Piva, *Calcif. Tissue Int.*, 2017, **101**, 341-354.

13. M. T. Raimondi, S. M. Eaton, M. Lagana, V. Aprile, M. M. Nava, G. Cerullo and R. Osellame, *Acta Biomater.*, 2013, **9**, 4579-4584.

14. F. Miculescu, A. Maidaniuc, S. I. Voicu, V. K. Thakur, G. E. Stan and L. T. Ciocan, *ACS Sustain. Chem. Eng.*, 2017, **5**, 8491-8512.

15. L. H. Fu, C. Qi, Y. J. Liu, W. T. Cao and M. G. Ma, *Sci. Rep.*, 2018, **8**, 8292.

16. A. Szczes, L. Holysz and E. Chibowski, *Adv. Colloid Interface Sci.*, 2017, **249**, 321-330.

17. S. Dutta, A. Bhaumik and K. C. W. Wu, *Energy Environ. Sci.*, 2014, **7**, 3574-3592.

18. J. Xiao, D. H. Mei, X. L. Li, W. Xu, D. Y. Wang, G. L. Graff, W. D. Bennett, Z. M. Nie, L. V. Saraf, I. A. Aksay, J. Liu and J. G. Zhang, *Nano Lett.*, 2011, **11**, 5071-5078.

19. Z. C. Wu, K. Tian, T. Huang, W. Hu, F. F. Xie, J. J. Wang, M. X. Su and L. Li, *ACS Appl. Mater. Interfaces*, 2018, **10**, 11108-11115.

20. T. Huang, Z. C. Wu, Q. Yu, D. G. Tan and L. Li, *Chem. Eng. J.*, 2019, **359**, 69-78.

21. Z. S. Liu, P. Jiang, G. Huang, X. W. Yan and X. F. Li, *Anal. Chem.*, 2019, **91**, 3659-3666.

22. H. R. R. Ramay and M. Zhang, *Biomaterials*, 2004, **25**, 5171-5180.

23. S. K. Hubadillah, M. H. D. Othman, Z. S. Tai, M. R. Jamalludin, N. K. Yusuf, A. Ahmad, M. A. Rahman, J. Jaafar, S. H. S. A. Kadir and Z. Harun, *Chem. Eng. J.*, 2020, **379**, 122396.

24. H. Bai, F. Walsh, B. Gludovatz, B. Delattre, C. L. Huang, Y. Chen, A. P. Tomsia and R. O. Ritchie, *Adv. Mater.*, 2016, **28**, 50-56.

25. K. A. Gross and K. A. Bhadang, *Biomaterials*, 2004, **25**, 1395-1405.

26. S. Y. Chen, B. H. Zhou, W. L. Hu, W. Zhang, N. Yin and H. P. Wang, *Carbohydr. Polym.*, 2013, **92**, 1953-1959.

27. C. Busuioc, C. D. Ghitulica, A. Stoica, M. Stroescu, G. Voicu, V. Ionita, L. Averous and S. I. Jinga, *Ceram. Int.*, 2018, **44**, 9433-9441.

28. Z. T. Xie, T. A. Asoh and H. Uyama, *Carbohydr. Polym.*, 2019, **214**, 195-203.

29. Y. R. Xin, Q. C. Xiong, Q. H. Bai, M. Miyamoto, C. Li, Y. H. Shen and H. Uyama, *Carbohydr. Polym.*, 2017, **157**, 429-437.

30. G. W. Jackson and D. F. James, *Can. J, Chem. Eng.*, 1986, **64**, 364-374.

31. K. N. Li, J. N. Wang, X. Q. Liu, X. P. Xiong and H. Q. Liu, *Carbohydr. Polym.*, 2012, **90**, 1573-1581.

Concluding Remarks

In this doctoral thesis, hierarchically porous inorganic materials were fabricated by using the cellulose materials and commercial cellulose-based materials as templates. Specifically, the cellulose monolith prepared *via* TIPS will be used as the main template in this research, and then different monolithic inorganic materials were prepared.

In Chapter 1, hydrophilic and hierarchically porous inorganic monolith was prepared by using an ecofriendly cellulose material as a template. The cellulose monolith template was prepared from cellulose acetate by a thermally induced phase separation method. The silica was then prepared in the presence of the cellulose monolith by a typical sol-gel reaction of tetraethyl orthosilicate (TEOS) to form the composite monolith, which was converted to the silica monolith by burning in air to remove the cellulose monolith. Owing to the hierarchically porous structure of the cellulose monolith template, the obtained silica monolith showed a similar hierarchically porous structure. The pore structure could be controlled by changing the fabrication parameters, such as the kind of cellulose monolith and TEOS concentration. The surface-modified silica monolith was developed for further applications, which was also investigated in this Chapter. Moreover, the recycled cigarette filters are deacetylated to cellulose filters (CFs), which are then applied as a template to prepare fiber-like inorganic oxides (titanium dioxide: TiO_2 and silicon dioxide: SiO_2). Owing to the fibrous structure of the CF template, the obtained inorganic oxides (TiO_2 and SiO_2) show a similar fiber-like structure. Furthermore, the TiO_2 fiber-like materials are evaluated for their photocatalytic properties by analyzing their effect on the degradation of methylene blue (MB) as model pollutants.

In Chapter 2, hierarchically porous TiO_2 monolithic materials are potential candidates for water remediation, as they are easy to recover and can be used in flow systems. In this study, we used an ecofriendly cellulose material as a template to prepare a hierarchically porous TiO_2 monolith. The cellulose monolith template was prepared from cellulose acetate by a thermally induced phase separation method. A composite monolith was then prepared in the presence of the cellulose monolith by a typical sol–gel reaction of titanium isopropoxide

(TTIP). This composite monolith was then converted to a TiO_2 monolith by burning in air to remove the cellulose monolith. Owing to the hierarchically porous structure of the cellulose monolith template, the obtained TiO_2 monolith showed a similar hierarchically porous structure, as confirmed by scanning electron microscopy and nitrogen adsorption–desorption analyses. The pore structure could be controlled by changing the fabrication parameters, such as the type of cellulose monolith and TTIP content. The photocatalytic performance of the TiO_2 monolith was evaluated by studying its effect on the degradation of methylene blue (MB) in flow system.

In Chapter 3, a hard template method was developed and a porous HA monolith with hierarchical pore structure, suitable porosity and pore size was successfully prepared. The cellulose monolith template was prepared from cellulose acetate by a thermally induced phase separation method. The cellulose monoliths were then immersed into the HA slurry with chitosan to form the composite monolith, which was converted to the HA monolith by burning in air to remove the chitosan and cellulose monolith. Owing to the hierarchically porous structure of the cellulose monolith template, the obtained HA monolith showed a similar hierarchically porous structure, as confirmed by scanning electron microscopy and nitrogen adsorption-desorption analyses. Furthermore, the as-prepared HA monolith was explored to study the adsorption property of bovine serum albumin (BSA), and the adsorption evaluation indicated that HA monolith has a high adsorption capacity of BSA.

In summary, these fabrication strategies established in this thesis provide a guidance for the future fabricate hierarchically porous inorganic materials based on biodegradable monolithic cellulose materials or commercial cellulose-based materials. I also believe that the prepared hierarchically porous inorganic materials are promising in other application and further modification.

List of Publications

1. Hierarchical silica monolith prepared using cellulose monolith as template

Yanting Lyu, Taka-Aki Asoh*, and Hiroshi Uyama*

Polymer Degradation and Stability, **2020**, *177*, 109164.

DOI: https://doi.org/10.1016/j.polymdegradstab.2020.109164

2. Hierarchically porous TiO_2 monolith prepared using a cellulose monolith as a template

Yanting Lyu, Taka-Aki Asoh*, and Hiroshi Uyama*

Materials Chemistry Frontiers, **2021**, *5*, 3877

DOI: 10.1039/d1qm00220a

3. Fabrication of Inorganic Oxide Fiber Using a Cigarette Filter as Template

Yanting Lyu, Taka-Aki Asoh*, and Hiroshi Uyama*

ACS Omega **2021**, *6*, 15374–15381

DOI: 10.1021/acsomega.1c01750

4. A Facile Synthesis of Three-dimensional Hydroxyapatite Monolith for Protein Adsorption

Yanting Lyu, Taka-Aki Asoh*, and Hiroshi Uyama*

In Preparation

Acknowledgments

This study was carried out from 2018 to 2021 at Department of Applied Chemistry, Graduate School of Engineering, Osaka University. During the 3 years, I have received a lot of assistant from many people around me. Upon the completion of this thesis, I am grateful to those who have offered me encouragement and support.

Firstly, I would like to express my sincere gratitude to my advisor Prof. Hiroshi Uyama for the continuous support of my Ph.D. study and related research, for his patience, motivation, and immense knowledge. His guidance helped me in all the time of research and writing of this thesis.

Besides my advisor, I would like to thank the rest of my thesis committee: Prof. Satoshi Minakata and Prof. Nobuhito Imanaka, for their insightful comments and encouragement, but also for the hard question which incented me to widen my research from various perspectives.

I also want to express my heartfelt appreciation to Assoc. Prof. Taka-Aki Asoh for his help in my research. Thank him for the manuscripts revising, inspirations, and experience sharing. He taught me the philosophy for overcoming the problem and encouraged me to build a strong heart when confronted with the challenge on the route of pursuing doctor degree. All these will be a great help to my future academic research and daily life.

My sincere thanks also go to Assistant Prof. Yu-I Hsu, Dr. Xinnan Cui, and Dr. Yasushi Takeuchi for their kind help and expert advice.

Special thanks also send to Ms. Yoko Uenishi and Ms. Tomoko Shimizu for their warm-hearted support in the laboratory affairs and the kind help in my daily life.

My appreciation also goes to the previous and current fellows in the laboratory: Dr. Zhaohang Yang, Dr. Masatoshi Kato, Dr. Chen Qian, Dr. Zhengtian Xie, Dr. Yankun Jia, Dr. Shunsuke Mizuno, Dr. Toshiki Tamiya, Dr. Bozhi Chen, Mr. Naharullah Bin Jamaluddin, Mr. Raghav Soni, Ms. Hanyu Wen, Mr. Akihide Sugawara, Mr. Mark Adam Malaluan Ferry, Ms. Yan Wang, Mr. Luwei, Zhang, Ms. Meng Wei, Mr. Yuxiang Jia, Mr. Nontarin Roopsung, Mr. Emil Hajili, Ms. Madhurangika Panchabashini Horathal Pedige, Ms. Yuka Kashihara, Mr. Yuji Kiba, Mr. Takeshi Hiraoka, Mr. Yuki Shioji, Mr. Atsushi Koizumi, etc. Thanks for their kind-hearted help both in my research and daily life.

I would like to thank the scholarship support from China Scholarship Council (CSC) for my academic study and stay in Japan. Their committee and staff offered me help and encouragement along the way and inspired me with their goodness.

Last but not the least, I would like to thank my family for supporting me spiritually throughout writing this thesis and my life in general. This thesis would not have been possible without their help, love, dedication, and encouragement.

June 2021

LYU YANTING